

BACHELOR

Etching of trenches for Marjorana braiding networks

Choi, Kevin

Award date:
2017

[Link to publication](#)

Disclaimer

This document contains a student thesis (bachelor's or master's), as authored by a student at Eindhoven University of Technology. Student theses are made available in the TU/e repository upon obtaining the required degree. The grade received is not published on the document as presented in the repository. The required complexity or quality of research of student theses may vary by program, and the required minimum study period may vary in duration.

General rights

Copyright and moral rights for the publications made accessible in the public portal are retained by the authors and/or other copyright owners and it is a condition of accessing publications that users recognise and abide by the legal requirements associated with these rights.

- Users may download and print one copy of any publication from the public portal for the purpose of private study or research.
- You may not further distribute the material or use it for any profit-making activity or commercial gain

Etching of trenches for Majorana braiding networks

Kevin Choi (0889741)

June 29, 2017

Abstract

This report researches the etching of trenches in InP {001} substrates to grow nanowires (NW's) for Majorana braiding networks. Two etching methods are used in the experiments: wet chemical etching and in-situ MOVPE etching. In both etching processes, smooth {111}B facets have to be exposed, because this is required to properly grow NW's.

For wet chemical etching, the trench width and height have been measured for variable mask openings after etching for 30 s with a 1:3 buffered HBr:H₃PO₄ solution at room temperature (20 °C). Two regions can be found in the results, trenches where there is no {001} facet present (V-grooves) and trenches where a {001} facet is present (U-grooves). For V-grooves, the found width to height ratio is 1.55 ± 0.04 , which is larger than the expected value of $\sqrt{2} \approx 1.41$. Two angular method corrections have been suggested to correct the measured width and height. Both methods, however, do not give a significant difference with the uncorrected measurements, because the corrections are small compared to the measurement uncertainties. A more likely explanation for the high width to height ratio is that the SEM images are contracted in the height due to charging effects.

For in-situ MOVPE etching, trenches of two samples situated at the edge and center of the rotation disk are examined. Etching is done with 5 cc HCl gas, at a temperature of 625 °C for 15 min. Both samples have trench openings of 180 nm and 200 nm. Results show that the center samples have a width to height ratio of 1.414 ± 0.005 and 1.413 ± 0.009 for 180 nm and 200 nm openings respectively, which is in agreement with the expected value. However, the edge samples, which should produce the same results, have width to height ratios that are higher than expected: 1.1469 ± 0.0060 and 1.460 ± 0.009 for 180 nm and 200 nm openings respectively. This was caused by the fact that the width is higher than expected, which excludes that the difference is caused by height contraction of the image. Possible explanations is that SEM images were expanded along the width, the presence of a small {001} facet, or a different etching speed at the side facets due to the difference in local airflow.

Analyzing trench width and height are important for the positioning of gold droplets for NW growth. SEM images have been mapped in an AutoCAD model in order to check if these gold droplets are placed accordingly. The example model discussed in this report shows that some droplets may need to be placed closer to the trench opening.

More research should be done to optimize the etching process of trenches. It is very useful to see if etch rate remains constant over time and if variation in temperature affect the etch rate according to theory. More important is to check for what parameters the surface morphology of the trenches are good or bad. The SEM as measurement equipment deserves attention as well, since it is not always clear how it affects the width and the height of the pictures.

Contents

1	Introduction	2
2	Theory	4
2.1	Indium phosphide	4
2.2	Trench etching process	5
2.3	Wet chemical etching	6
2.4	In-situ MOVPE etching	8
2.5	Model for anisotropic etching	10
3	Experiment	13
3.1	Samples	13
3.2	Measurement corrections	13
3.3	MOVPE etching at center and edge of rotation disk	15
3.4	Mapping in the AutoCAD model	15
4	Results and discussion	16
4.1	Effect measurement corrections on width to height ratio	16
4.2	MOVPE etching at center and edge of turning table	17
4.3	Mapping in the AutoCAD model	17
4.4	New kit issue of the MOVPE reactor	18
5	Conclusion	21
A	Width height ratio of V-grooves	26
B	Derivation of Shaw's formula on etch rate	27
C	The Newton-Raphson method	29
C.1	MATLAB scripts	30

Chapter 1

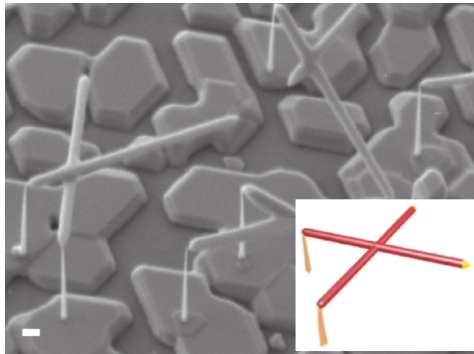
Introduction

Nanowires (NW's) with topological properties provide possibilities to create braiding networks for Majorana Zero Modes (MZM's). It is theoretically predicted that MZM's exist when a one-dimensional III-V semiconductor NW is brought into contact with a conventional superconductor [1, 2] and their signatures have also been detected in experiments [3–6]. InSb is considered the best material for these NW's because it has a large Landé-g factor [7], and a strong spin-orbit interaction (SOI) [8, 9], which are essential properties to realize MZM's. Several Majorana braiding schemes for quantum computing have been proposed [10–15]. The exact workings of these schemes are beyond the scope of this report, but these schemes will affect how the NW networks should be fabricated. For example, Hyart and Aasen's braiding scheme requires to form one or more single-crystalline NW junctions.

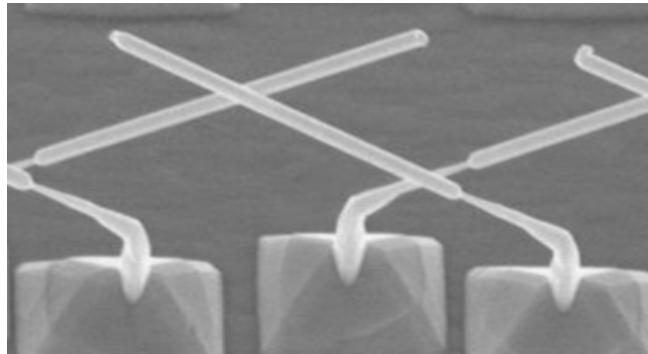
One of the first methods to fabricate NW networks to realize MZM's is suggested by Plissard et al. [16] and is shown in figure 1.1a. In order to realize these NW networks, uniform InP and InAs stems are grown. In the next step, these stems are thermally annealed so that the InSb NW will grow on a side facet of the stem. If a pair of NW's grow on the correct facet, they will merge and form a T- or X-shaped network. Plissard et al. have shown that this method gives a yield of 8%, taking into account if two wires merge under an optimal angle of 70.5° so that they can form a single-crystalline junction.

A better method with a theoretical yield of 25% (for networks with a single junction) is suggested by Car et al. [17] and is shown in figure 1.1b. The idea is to grow InP stems, then let them kink into one of the two possible $\langle 111 \rangle_B$ directions (see also Wang et al. [18] for more details), and then continue the NW growth with InSb. In this way, it is guaranteed that the angle is optimal if two NW's cross. The yield, however, is limited due to the occurrence of twinning in the kinked InP stem. The junction of two NW's is only single-crystalline if the number of twins of the two stems belonging to these NW's are both even. Because the probability of getting even or odd number of twins is both 50%, the average final yield will be 25% [17].

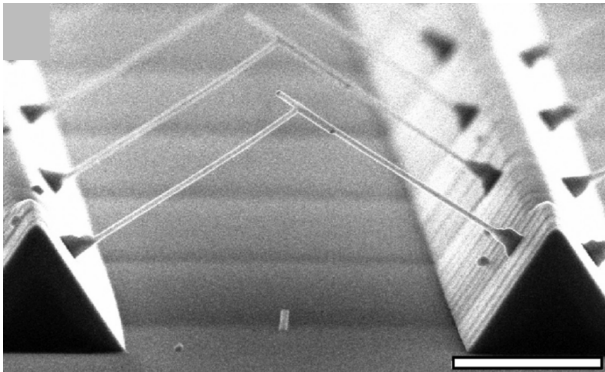
Another issue of the method described by Car et al. is that the direction in which the InP stem will kink is not controllable, complicating the construction of NW networks. An alternative method that can be used to omit the kinking process is given by Dalacu et al. [19], who grew InAs NW's on epitaxially grown InP ridges (see figure 1.1c). A more time efficient method to expose two opposing $\{111\}_B$ planes is to etch trenches in the substrate, which saves an additional epitaxial growth step to fabricate ridges [20–22] (see figure 1.1d). This report will focus on the fabrication of such trenches and two different etching methods (wet chemical etching and in-situ MOVPE etching) will be analyzed for different parameters. The theory behind the trench etching process and details of the two etching methods will be thoroughly discussed in chapter 2. In chapter 3, all the experiments that will be done are discussed. It provides an overview of all the samples that are examined, explains the instruments used, and addresses the procedures followed in the experiment. In chapter 4, all the results of the experiments mentioned in chapter 3 are presented and discussed and the final conclusions will be drawn in chapter 5.



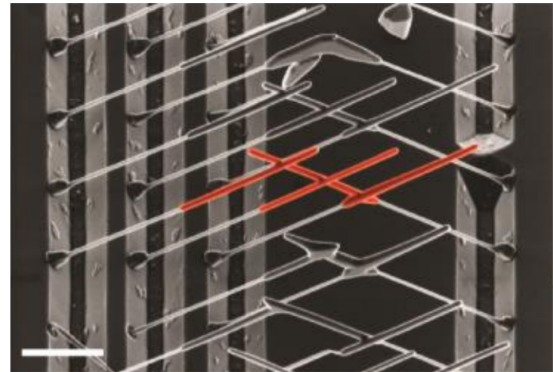
(a)



(b)



(c)



(d)

Figure 1.1: Examples of NW networks: (a) first attempt of growing NW networks for Majorana braiding operations by Plissard et al. [16]; (b) NW networks for Majorana braiding operations by Car et al. [17]; (c) NW networks grown on epitaxially grown InP ridges by Dalacu et al. [19]; (d) NW networks grown on wet chemically etched trenches by Gazibegovic et al. [22].

Chapter 2

Theory

2.1 Indium phosphide

The substrate on which the trenches will be fabricated is indium phosphide (InP). This material has a zinc blende (ZB) crystal structure (see figure 2.1), which is based on two fcc crystals that are displaced from each other by a quarter body diagonal in the direction of the body diagonal. An important characteristic of a ZB is that it has two types of $\{111\}$ -planes: $\{111\}$ A and $\{111\}$ B. This is because ZB $\{111\}$ -planes can either have group III atoms (In), the $\{111\}$ A plane, or group V atoms (P), the $\{111\}$ B plane as outermost layer. By convention, the family of $\{111\}$ B are all the planes that have an odd number of negative one indices, i.e. $(11\bar{1})$, $(\bar{1}\bar{1}\bar{1})$, etc. The two different types of $\{111\}$ -planes in ZB explains that InP has different properties in the $\langle 111 \rangle$ A and $\langle 111 \rangle$ B direction. To explain this in more detail, the different properties follows from the fact that group III atoms have three valence electrons while group V atoms have five. As a result, $\{111\}$ B planes have two additional electrons that can take part in chemical reactions [23, 24] and it is suggested that this is the reason why NW's preferably grow in the $\langle 111 \rangle$ B direction.

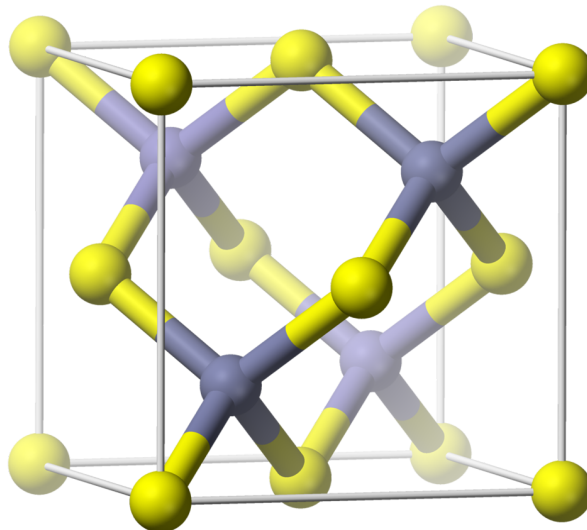


Figure 2.1: Visualization of a zinc blende unit cell.

2.2 Trench etching process

A simple etching process for trenches is visualized in figure 2.2. The first step is to deposit a silicon oxide (SiO_2) layer on the wafer. This is done by using plasma-enhanced chemical vapor deposition (PECVD).

The next step is to coat the wafer with e-beam resist. This resist layer works similar to photoresist: it will be rendered soluble (positive e-beam resist) or insoluble (negative e-beam resist) for development after exposure to electrons. Examples of (positive) e-beam resists are PMMA (poly-methyl methacrylate) [25] and ZEP 520 [26], which are both long chain polymers that will break in smaller and more soluble pieces when it is exposed to an electron beam.

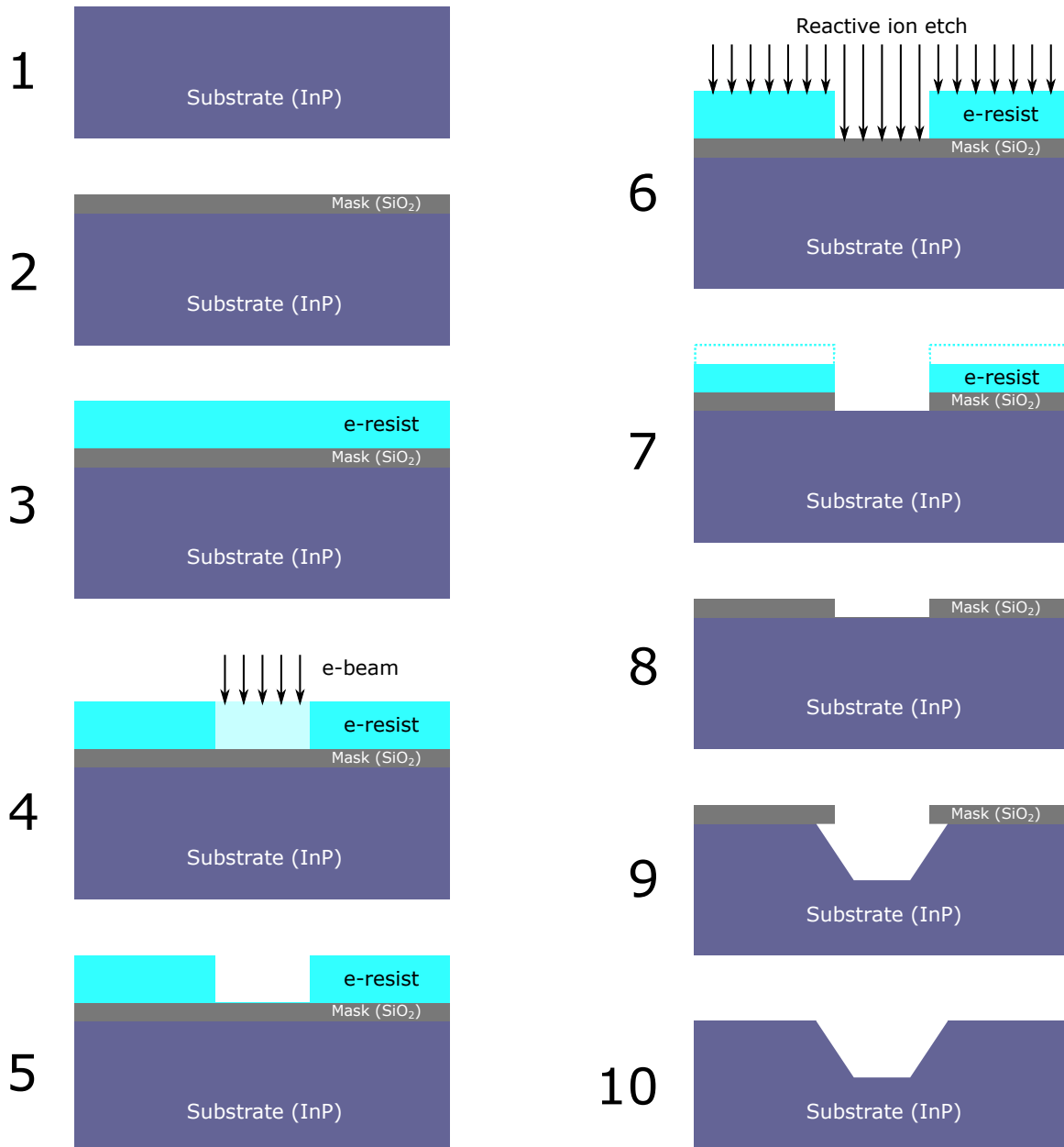


Figure 2.2: Visualization of the etching process of trenches: 1. an out of the box InP wafer; 2. a silicon oxide mask is deposited on the wafer using plasma-enhanced chemical vapor deposition (PECVD); 3. an e-beam resist layer is coated on the wafer; 4-5. By using e-beam lithography (EBL), openings for the trenches are printed; 6-7. A reactive ion etch (RIE) is used to remove the exposed silicon oxide mask. A part of the e-beam resist may be etched away as well, but will not reach the mask; 8. The e-beam resist is removed; 9. The trenches are etched at the mask opening; 10. The silicon oxide mask is removed.

After applying resist, e-beam lithography (EBL) will be used to print the opening of the trenches.

Modern EBL tools write patterns using a single electron beam and they write it directly without the use of a mask. Despite the fact that electrons repel each other, EBL tools can achieve a resolution of only a few nanometers [27, 28]. A drawback of a direct write EBL system, however, is that it may take a lot of time to draw complex patterns, although there exist techniques to resolve this such as parallel electron beams [29]. One important issue is that trench opening usually end up wider than the opening according to the model. The wider opening is caused by forward [30, 31] and backward scattering [32] of the electrons.

After development of the resist, the exposed SiO_2 will be removed with reactive ion etching (RIE). RIE is a dry etching method that uses chemically reactive plasma to remove deposited material from a wafer. In this step, it is important to etch the SiO_2 mask, without etching the InP substrate significantly. This can be realized by using a selective etchant for SiO_2 such as CHF_3 or a mixture of CF_4 with H_2 (a nice overview of selective etchants for different materials is given by Kurogi, table 1 [33]). Right after etching, the e-beam resist will be removed, which is done by an O_2 plasma.

The second final step is to use the opening in the silicon oxide mask to etch the trenches. In this report, two etching methods will be discussed and elaborated: wet chemical etching (section 2.3) and in-situ MOVPE etching (section 2.4). It is important that the $\{111\}\text{B}$ facets are exposed after etching, so the printed mask openings are along the $[110]$ direction. It is also vital that the vertical $(1\bar{1}0)$ walls are not visible, because this will cause problems when resist has to be deposited for the fabrication of the NW's. In case only $\{111\}\text{B}$ planes are present, the trench will have a V shape, which is called a V-groove. For ZB, V-grooves formed by $(111)\text{B}$ planes make an angle of 70.5° or equivalently,

$$\frac{w}{h} = \sqrt{2} \approx 1.41, \quad (2.1)$$

where w and h are the trench width and height respectively. The derivation of equation (2.1) will be explained in APPENDIX. In this report, trenches are called U-grooves if a (001) flat is present as well (together with the $\{111\}\text{B}$ ridges).

After the etching of the trenches, the SiO_2 mask will be removed. In the experiments discussed in chapter 3, this step may be omitted so that the mask opening can be measured and be compared with the opening that is given to the EBL tool.

2.3 Wet chemical etching

For wet chemical etching, a liquid etchant will be used to react with the substrate material. Because chemical reactions are involved in the etching process, the etch rate is bounded by the reaction rate. As a result, the etch rate r can be calculated by using the Arrhenius equation,

$$r = A \exp \frac{E_a}{k_B T}, \quad (2.2)$$

where E_a is the activation energy of the reaction, k_B is the Boltzmann constant, T is the temperature, and A is a constant for the specific reaction. The etch rate can also be determined by measuring the etched distance and divide it by the etching time. Some experiments on wet chemical etching have measured the etch rate as a function of the temperature and the results are in agreement with the Arrhenius equation [34].

In some cases, the etch rate is not limited by the reaction rate but (partially) by the diffusion of the etchant. An example of a diffusion-limited etchant is bromide methanol BrMe. Kappelt and Bimberg showed that the bottom of a trench etched with BrMe is convex (see figure 2.3), which is an indication that etching is diffusion-limited in the $\langle 001 \rangle$ direction [35]. On the other hand, the planar $\{111\}\text{A}$ facets are an indication that the etching is reaction-limited in the $\langle 111 \rangle\text{A}$ direction. Kappelt and Bimberg state that defects caused by diffusion-limited etching in the $\langle 001 \rangle$ direction are passed onto the $\{111\}\text{A}$ facets. Thus, diffusion limited etching should be avoided, because smooth $\{111\}\text{B}$ facets

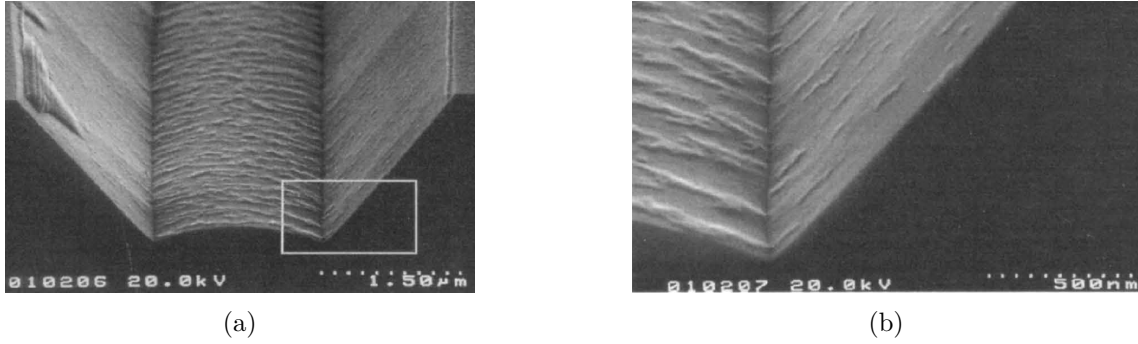


Figure 2.3: SEM images from Kappelt and Bimberg [35] etching with bromide methanol BrMe, with (a) the overall situation and (b) a zoomed image of the area indicated by the mark in (a). The convex bottom of the trench is an indication that the etch rate in the $\langle 001 \rangle$ direction is diffusion-limited.

are required for the NW growth step, although an additional etching step may help to remove any defects.

Adachi and Kawaguchi have done very extensive research on the chemical etching characteristics of InP for various etchants [36]. The SiO_2 mask of the samples have strip openings along the $[110]$ direction. Because $\{111\}B$ planes are used to grow NW's, the etchants that expose these planes are of great interest. This is the case for several solutions of the HCl, and the HBr system, and some examples are displayed in figure 2.4. Adachi and Kawaguchi suggest that the different etching profiles are a result of different etching rates for different crystallographic directions. This means that crystallographic planes with a low etching rate will be mainly visible in the etching profile.

An explanation of the anisotropic phenomenon of wet chemical etching is given by Wang et al. [37]. The etch rate in a specific crystallographic direction depends on how reactive the corresponding crystallographic planes are. For example, $\{001\}$ planes are double dangling bond and this makes them more reactive compared to $\{111\}$ planes that only have a single dangling bond. Moreover, the etch rate of $\{111\}A$ planes is sometimes much lower than that of $\{111\}B$ planes. The explanation is the same as that of why NW's preferably grow in the $\{111\}B$ direction (see section 2.1): the two extra valence electrons of the group V atoms make $\{111\}B$ planes more reactive than $\{111\}A$ planes [23]. This is in particular the case of etchants that contain oxidizing agents and the etch rate of $\{111\}B$ planes may even match that of $\{001\}$ planes. The etch rate of $\{1\bar{1}0\}$ planes usually lies somewhere between that of $\{111\}A$ and $\{111\}B$ planes. Like the $\{111\}A$ and $\{111\}B$ planes, they have a single dangling bond. The difference, however, is that they contain both group III and group V atoms and thus the etch rate should lie somewhere between that of $\{111\}A$ and $\{111\}B$ planes. Thus, given the explanation above, the etching rates r for exchange-type reactions (so no oxidation/reduction is involved) are ordered as follows:

$$r(\{001\}) > r(\{111\}B) > r(\{1\bar{1}0\}) > r(\{111\}A). \quad (2.3)$$

Experiments conducted by Wang et al. confirm this order of etch rates for $5\text{HCl}:1\text{H}_3\text{PO}_4$.

Pictures from both Adachi and Kawaguchi and Wang et al. show the presence of a vertical $\{1\bar{1}0\}$ facets for $1\text{HCl}:1\text{H}_3\text{PO}_4$ and $5\text{HCl}:1\text{H}_3\text{PO}_4$ etchants respectively. As explained in section 2.2, these facets are unwanted and they should not be formed. One method to do this is to make use of photoresist masks to control the undercutting. Huo et al. showed that undercut etching with $5\text{HCl}:1\text{H}_3\text{PO}_4$ can be increased by using higher dehydration or postbake temperatures [38], which is needed to prevent the formation of $\{1\bar{1}0\}$ facets in the etching process. An increased undercut can be explained by a thicker native oxide layer on the InP substrate. Studies have shown that high temperatures and/or exposure to water increase the thickness of this layer [39, 40]. For SiO_2 masks, however, the method described by Huo et al. does not have a significant effect on the amount of undercut. Other methods that do work for SiO_2 masks are invented by Dautremont-Smith and Wilt, which makes use of plasma or thermal oxidation to create a native oxide layer [41]. Another way to prevent $\{1\bar{1}0\}$ facets is to use the

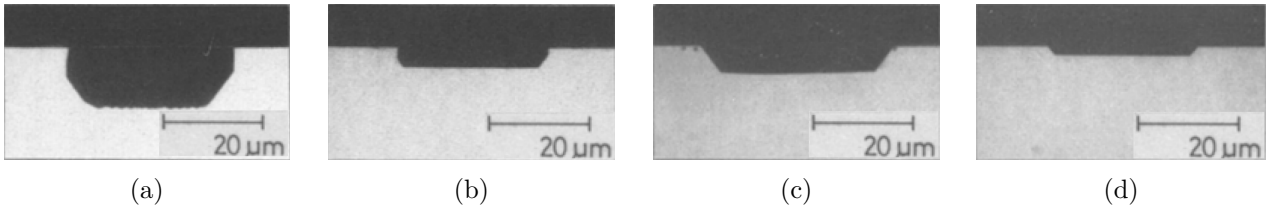


Figure 2.4: Etching profiles for (a) HCl, (b) HCl:H₃PO₄, (c) HBr, and (d) HBr:H₃PO₄ from Adachi and Kawaguchi [36].

HBr system instead of the HCl system, considering Adachi and Kuwaguchi's research. Unfortunately, the amount of research on HBr as etchant for InP is limited compared to HCl.

It is desired to have control over the (relative) etch rate for different crystallographic planes. A common method to control these etch rates is by changing the H₃PO₄ content of the etchant. The research of Adachi and Kuwaguchi shows that the addition of H₃PO₄ to HCl (and also HBr) does not significantly affect the etching profile, but it does reduce the etch rate of the {001} plane. For high H₃PO₄ content with respect to HCl, the relative etch rate of the {111}B plane with respect to the {001} plane will increase, resulting in arrow or rectangular shaped trenches [42, 43]. Another possibility to control the etching is the usage of sacrificial and stopping layers, discussed by Hjort [44]. This is useful when, for example, it is desired to have a {001} plane at a certain depth. If the InP is used as a sacrificial layer, then InGaAs can be used as stopping layer, since the selectivity of InP over InGaAs is practically infinite for HCl based etchants such as HCl:H₂O [45].

For HCl based solutions, Notten suggested that etching takes place by the following reaction [46]:



It is suggested that this reaction takes place in two steps: first, a single HCl and InP molecule exchanges their bonds to form In–Cl and P–H bonds. The second step goes similar to the first step, but takes place at a higher rate due to decreased stability after the first step. In the end, InCl₃ will be hydrolyzed and PH₃ will leave the solution as a gas. A visualization of this reaction is given by Cuypers et al. [47] and is shown in figure 2.5.

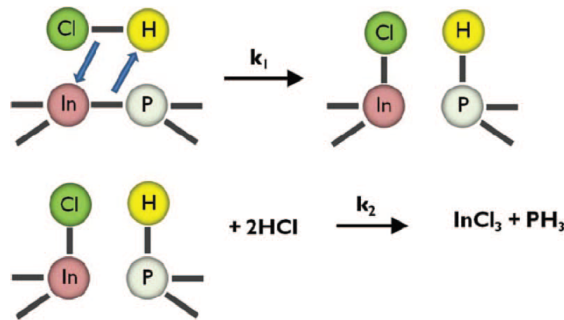


Figure 2.5: Visualization of chemical etching of InP using HCl suggested by Notten [46] (figure from Cuypers et al. [47]).

2.4 In-situ MOVPE etching

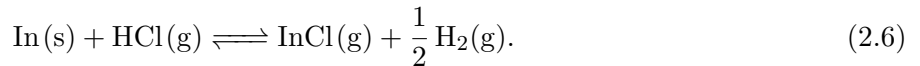
Metalorganic vapour phase epitaxy (MOVPE) – sometimes called organometallic vapour phase epitaxy (OMVPE) or metalorganic chemical vapour deposition (MOCVD) – is one of the methods that can be used to grow NW's. It is also possible to do the trench etching process right before the epitaxial growth in a MOVPE reactor, which is called in-situ MOVPE etching (or MOVPE etching in short).

For the application of braiding networks, NW growth will not be done right after MOVPE etching, because gold droplets have to be deposited first. One of the first etching gases that was reported is HCl, which was used to polish the substrate before epitaxial growth [48]. Other etching gases that were reported are tertiarybutylchloride (TBCl) [49–51], phosphorus trichloride (PCl₃) [52, 53], and ethylene dibromide (EDB) [54].

One of the first reports on etching of V-grooves in InP was given by Caneau et al. [55] The experiment was done by using a (001) oriented, S-doped InP substrates. Caneau found very good surface morphologies at a temperature of 625 °C if the partial pressure of the HCl etchant was low (0.021 mbar) and the etch depth does not exceed 3 μm. Furthermore, PH₃ should be present to prevent any thermal damage to the substrate, which would degrade the surface morphology. One of the samples in the experiments had a SiO₂ mask with stripe openings along the [110] direction. After etching, V-grooves with smooth {111}B planes have been rendered, which would be ideal for the NW growth step. The formation of {111}B planes also imply that the etching is reaction rate limited, and thus Arrhenius equation (equation (2.2)) can be used.

The fact that V-grooves are formed implies that the etch rate of {111} planes is much lower than that of {001} and {110} planes. A possible explanation can be found by using Sangster’s model of III-V ZB compound growth [56]. This model states that growth should not lead to an increase of the number of dangling bonds. This means that growth in the [001] and [110] direction needs only one atom, while growth in the <111> requires 4 atoms. If these requirements also apply for etching, then etching in the <111> direction requires to remove 4 atoms at once and thus the etch rate of {111} planes is much slower.

MOVPE etching with HCl is also discussed by Agnello and Ghandhi [48], who propose two different processes. The first proposal is that thermal decomposition plays a role in the etching process. P₂ will evaporate from the InP and the remaining non-volatile In will be removed by the HCl etchant according to



The other possibility is that etching occurs directly according to



Caneau et al., on the other hand, suggested that not P₄, but P₂ is formed in the etching process. Other literature seems to use this suggestion as well [57].

Agnello and Ghandhi state that the limiting factor of etching is the removal of InCl gas. Fast removal of InCl will be important in order to acquire good surface morphologies. This can be acquired by using intermediate temperatures of around 650 °C, and low HCl pressures of around 0.020 mbar. Intermediate temperatures are necessary because low temperatures do not properly remove InCl and high temperatures cause too much thermal decomposition. Low HCl pressures are important, because high pressures will enhance thermal decomposition, despite the fact that HCl is needed to form InCl. These requirements are in agreement with research from Caneau et al. discussed earlier, who found a smooth surface morphology in similar conditions (temperature of 625 °C, etch time of 30 s, and a partial pressure of HCl of 0.021 mbar). A difference in the two situations, however, is that Agnello and Ghandhi uses H₂/AsH₃ instead of PH₃.

Caneau et al. and Agnello and Ghandhi also reported findings on the relation of the etch rate with other parameters. The relation between partial pressure HCl and the etching rate seems to depend on the ambient gas that is used. For a H₂/AsH₃ environment, the relations seems linear, whereas the relations seems sub-linear for PH₃ environments (see figures 2.6a and 2.6b respectively). Furthermore, Caneau et al. also found that the etch rate remains constant over time.

More recent research has been done on in-situ MOVPE etching of InP. Tsuchiya et al. etched next to InP various other alloy materials, such as InGaAs, InGaAlAs, and InAlAs [57]. Using a SiO₂ mask

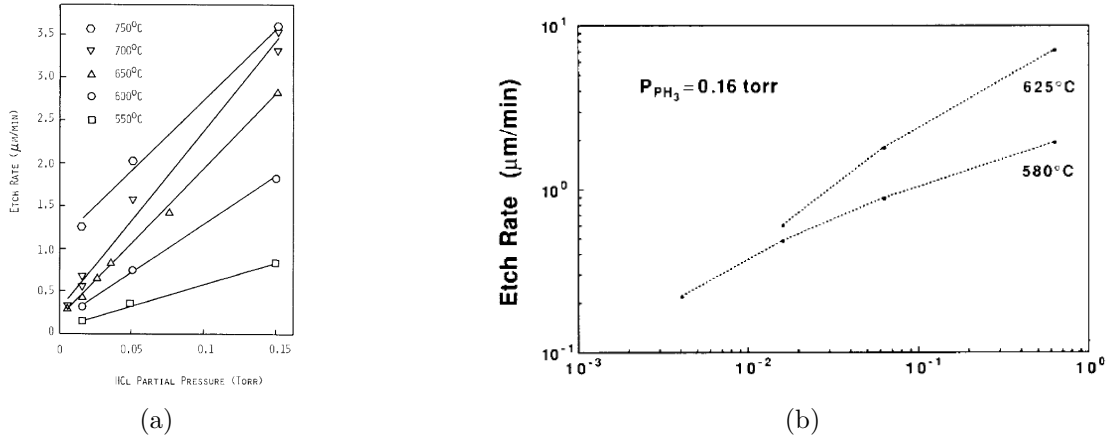


Figure 2.6: Plots of the etching rate versus the HCl partial pressure for (a) H_2/AsH_3 ambients [48], and (b) PH_3 ambients [55].

along the [110] direction, a smooth, mirror-like surface morphology has been found for InP for an etching temperature of 580°C and a HCl flow rate of $1.6 \times 10^{-4} \text{ mol min}^{-1}$. Kitatani et al. tested several etching recipes for materials with different compositional wavelengths including InP [58]. For all recipes, the surface morphology of InP was good, but for low etching temperatures (500°C), a relatively large undercut of approximately $1 \mu\text{m}$ has been found. This may be not suitable, because two trenches next to each other may merge as a result.

2.5 Model for anisotropic etching

As discussed in sections 2.3 and 2.4, both wet etching and MOVPE etching may show anisotropic etching profiles. A simple, but useful model to describe reaction-limited etching profiles is given by Klockenbrink et al. [34], who proposed to express the (minimum) etch rate as a function of the angle. A visualization of the minimum etch rates $r(\Theta)$ in several directions is given in figure 2.7. The figures shows that etch rates can be described by vectors that have its origin at the edge of the mask. Note that the left edge should be used for the etching planes on the left ($\Theta > 0$) and that the right edge for the etching planes on the right ($\Theta < 0$). The length of the vector indicates the maximum possible etch rate given the etching profile. In fact, the minimum etch rate in a specific direction is the actual distance between head and origin of the vector, divided by the etching time. The reason why it is called ‘minimum etch rate’ rather than ‘etch rate’ is because the actual etch rate in a specific direction may be higher. The actual etch rate is not always visible in the etching profile because the etching may be hindered by planes with a slow etch rate. However, because of how Klockenbrink’s model is defined, the minimum etch rate of a plane is equal to the actual etch rate if that plane is visible in the etching profile.

Calculation of the etch rate $r(\Theta)$ for the visible planes is a matter of calculating the perpendicular distance between point and line:

$$r(\Theta) = \frac{|(y_2 - y_1)x_0 - (x_2 - x_1)y_0 + x_2y_1 - y_2x_1|}{t\sqrt{(y_2 - y_1)^2 + (x_2 - x_1)^2}}, \quad (2.8)$$

where (x_0, y_0) indicate the coordinates of the origin, (x_1, y_1) and (x_2, y_2) are the coordinates of the two points that indicate a visible plane in the etching profile, and t is the etching time. The minimum etch rate $r(\Theta_i)$ of planes between two visible planes with corresponding angles Θ_1 and Θ_2 is given by Shaw [59] and is calculated according to

$$r(\Theta_i) = \frac{r(\Theta_1) \sin(\Theta_2 - \Theta_i) + r(\Theta_2) \sin(\Theta_i - \Theta_1)}{\sin(\Theta_2 - \Theta_1)}, \quad (2.9)$$

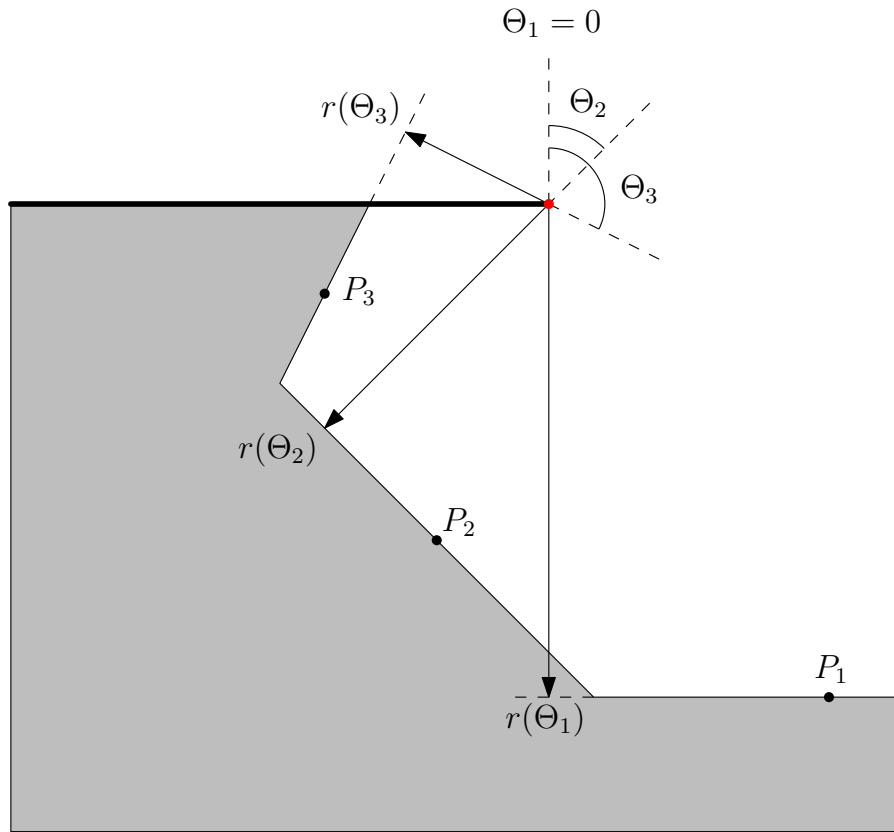


Figure 2.7: Visualization of the minimum etch rate $r(\Theta)$ for different angles $\Theta_1 = 0$, Θ_2 and Θ_3 . The etch rate can be described by a vector with a origin at the edge of the mask. The length of the vector equals the maximum allowed etch rate given the etch profile. The minimum etch rate of a plane equals the actual etch rate if there is a point (e.g. P_1 , P_2 and P_3 for the angles $\Theta_1 = 0$, Θ_2 and Θ_3 respectively) in the etching profile that has this plane as tangent, i.e. the plane itself is visible in the profile.

where $\Theta_1 \leq \Theta_i \leq \Theta_2$. A derivation of this expression can be found back in appendix B. In figure 2.8, some example diagrams of $r(\Theta)$ for different etching profiles are displayed.

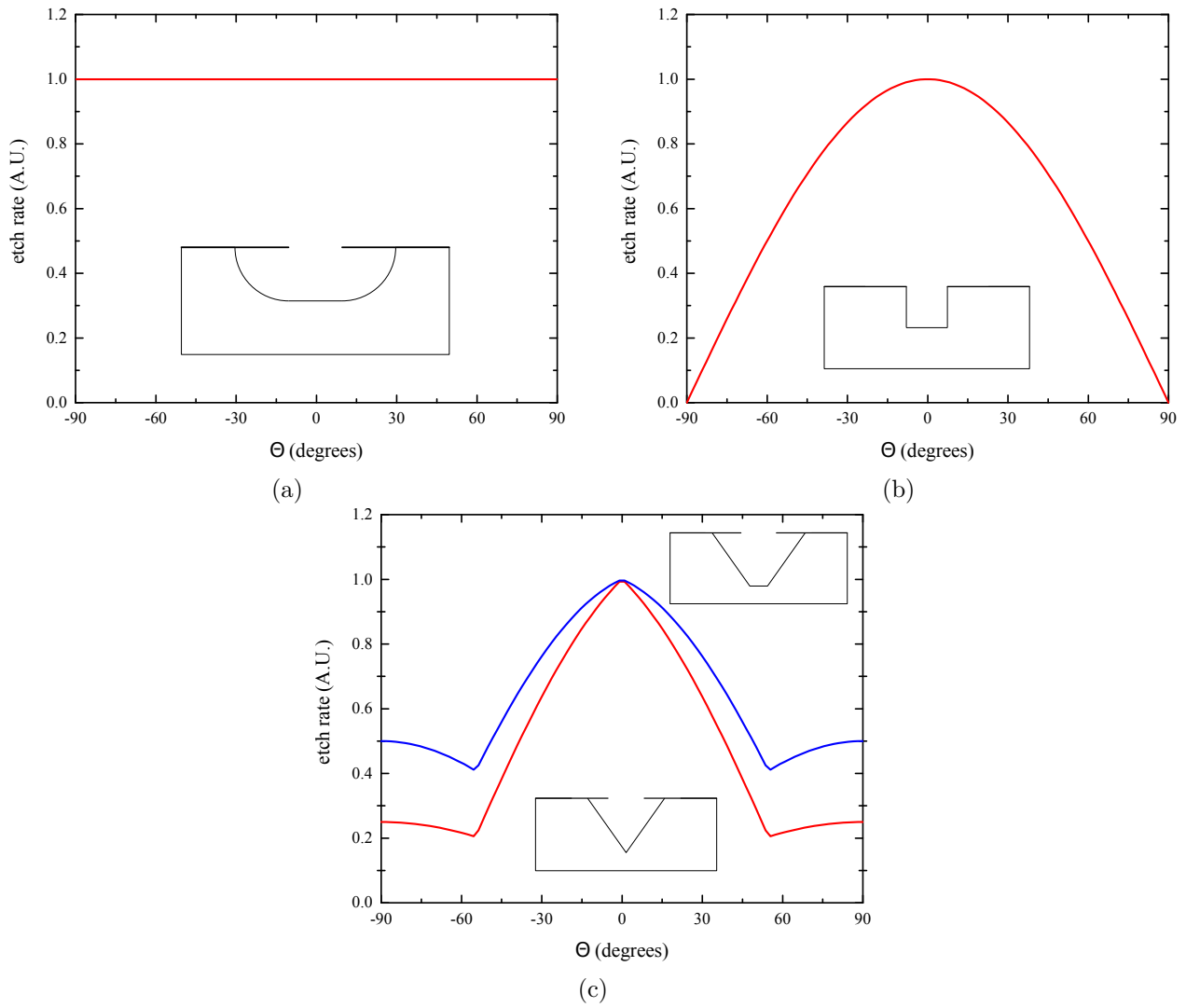


Figure 2.8: Theoretical etch rate versus angle diagrams for (a) isotropic profiles, (b) rectangular trenches, and (c) V-grooves (red) or U-grooves (blue).

Chapter 3

Experiment

3.1 Samples

In the experiments, the following samples are used and may be referenced as numbers in the rest of the report:

- (1) Trenches created by wet chemical etching with a 1:3 buffered HBr:H₃PO₄ solution. The etching is done for 30 s at room temperature (20 °C). The widths given in the model are varying from 400 nm to 800 nm with steps of 50 nm.
- (2) Trenches created by in-situ MOVPE etching with a 5 cc HCl flow. The etching is done for 15 min at a temperature of 625 °C. The width given in the model are either 180 nm or 200 nm.
- (3) The same as in sample (2), but the sample is positioned at the edge of the turning table of the MOVPE reactor instead of the center.
- (4) Trenches created by the same recipe as in (2) and (3), but these were fabricated at a different moment.

3.2 Measurement corrections

The software of the SEM provides a ruler tool to measure the width and height of the trenches. The advantage of SEM images is that they are an orthogonal projection: the magnification is not dependent on the distance between the detector and sample. However, measurements of the width and height have systematic errors if the surface of the sample is not perfectly perpendicular to the electron beam of the gun. Another cause of systematic errors is that trenches may not always be cleaved perfectly perpendicular. The systematic errors described here can be expressed by three angles, which will be called correcting angles. Note that this only applies to cross-section SEM images of the trenches. The first two correcting angles θ and ϕ describe how the sample is oriented in the SEM (see figures 3.1a and 3.1b). In this experiment, θ can be controlled by configuring the stage angle of the SEM and is therefore a known variable. However, the carbon tape on which the samples are placed result in uncertainties in θ . ϕ depends on how the sample is eventually placed on the sample holder. In ideal case, this angle would be zero, but it is difficult to assure this in practice. The third correcting angle ψ of the trenches with respect to the normal of the cleaved surface (see figure 3.1b). It is expected, however, that this angle is negligible compared to the other correcting angles, because cleaving should cause to break the crystal bonds along the $\{110\}$ plane, with imperfections of only a few atomic layers.

Horizontal and vertical distances $\Delta x'$ and $\Delta y'$ that are measured with the ruler tool of the SEM

software must be corrected according to

$$\Delta x = \frac{\Delta x'}{\cos \phi}, \quad (3.1)$$

$$\Delta y = \frac{\Delta y'}{\cos \theta}, \quad (3.2)$$

where Δx and Δy are the corrected distances. Note that equation (3.2) only holds if the measurement is done at the $(\bar{1}10)$ -surface. For measurements on the (001) -surface in the y -direction, the \cos in equation (3.2) should be replaced by \sin . If the sample is tilted such that the trenches on the (001) -surface are visible, the angle $\alpha = \phi' + \psi'$ of the trench with respect to the normal of the cleaved surface can be measured (see figure 3.1c). Using the horizontal and vertical corrections, this angle can be used to determine ψ and the relation is given according to

$$\tan(\phi + \psi) = \tan(\phi' + \psi') \sin \theta. \quad (3.3)$$

ϕ and ϕ' are related in a similar way according to

$$\tan \phi = \tan \phi' \sin \theta. \quad (3.4)$$

The actual width of the trench w is related to the measured width w' according to

$$w = w' \frac{\cos \psi}{\cos \phi}. \quad (3.5)$$

The problem now is that there are 5 unknown variables (ϕ , ϕ' , ψ , ψ' , and w), but only 4 equations (equations (3.3) to (3.5) and $\alpha = \phi' + \psi'$). There are two methods that can resolve this. In the first method (method I), the width of the SiO_2 mask opening will be measured in a topview image, which can be used to set the value for w . This makes the number of unknown variables equal to 4 and the system of equations can be solved numerically. The number of equations and variables can be reduced to 3 by substituting $\alpha = \phi' + \psi'$. As a result, ψ' is no longer in the set of equations, but only ϕ and ψ are interesting for the experiment.

A simple numerical method to solve a system of nonlinear equations is the Newton-Raphson method. This method uses an initial guess of the solution and calculates a ‘better’ guess of the solution. The process will be repeated until the guessed solution converges to the correct solution. Because the unknown correcting angles ϕ , ϕ' , and ψ are usually small, a good initial guess would be $(\phi, \phi', \psi) = (0, 0, 0)$. However, this guess will cause problems in this method (see appendix C for more details). This can be resolved by setting $\psi > 0$ if $\alpha > 0$ and $\psi < 0$ if $\alpha < 0$. Of course, $|\psi|$ should be small for the initial guess and all the other correcting angles can be set to zero without problems. More details on how the Newton-Raphson method is used to calculate the correcting angles and how uncertainties will be determined can be found back in appendix C.

An alternative and more simple method (method II) to solve the system is to assume that $\psi = 0$. As stated earlier, this angle is expected to be negligible, because the imperfections of the cleaved $(\bar{1}\bar{1}0)$ plane are practically only a few layers. As a result, $\psi' = 0$ and the solution can be simplified to

$$\Delta x = \Delta x' \sqrt{1 + \tan^2 \alpha \sin^2 \theta}, \quad (3.6)$$

$$\Delta y = \frac{\Delta y'}{\cos \phi}. \quad (3.7)$$

To check if the two methods of correcting angles can reliably be applied to obtain more accurate results for the trench width and height, SEM images of the cross-section and top view of the trenches in sample (1) will be made. The stage will be tilted under an angle of $\theta = (3 \pm 1)^\circ$. Using these images, the angle α indicated in figure 3.1c will be measured. This can be done by the angle measurement tool provided by the SEM software or by a program such as ImageJ. This method will be applied to correct the measured trench width and height for V-grooves and to check if the width to height ratio has the expected value of $\sqrt{2}$ (see equation (2.1)). The results can be found back in section 4.1.

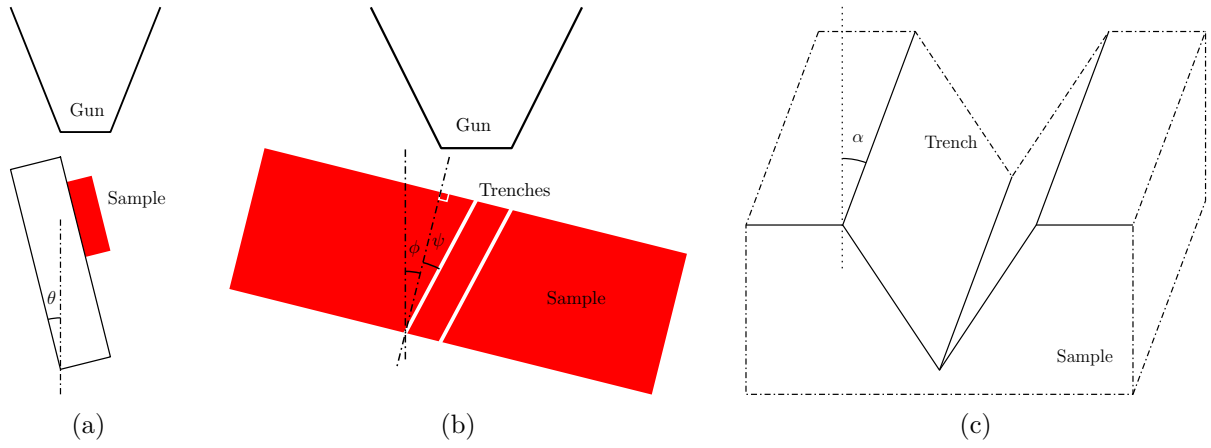


Figure 3.1: Visualization of the correcting angles θ , ϕ , ψ , and the angle α from the side of the sample (a), from the top of the sample (b) and from the point of view of the SEM (c).

3.3 MOVPE etching at center and edge of rotation disk

The samples on which trenches are fabricated in the MOVPE reactor are positioned on a rotation disk. This second experiment will investigate if samples positioned on the center of the rotation disk produce the same result as the ones positioned on the edge of the disk. Sideview and topview images of these samples will be made and compared and the stage is tilted under an angle of $\theta = (5 \pm 1)^\circ$. For both the 180 nm and 200 nm model openings, the mask opening, the width and the height will be measured. An instrumentally weighed average and standard error (SE) will be calculated for both model openings for both samples. These results will also be used to determine if the width to height ratio is close to the expected value of $\sqrt{2}$. Because it is expected that ϕ and ψ are negligibly small, only the height of the trenches will be corrected as explained in section 3.2. The final results are summarized in section 4.2.

3.4 Mapping in the AutoCAD model

The idea of analyzing the trench width and height is to pinpoint where the gold droplets for the NW growth process need to be placed. AutoCAD is used to model the position of the trench openings and the gold droplets. Topview SEM images can be imported in AutoCAD in order to see if the gold droplets are properly placed. An example with topview images of sample (4) will be shown in section 4.3.

Chapter 4

Results and discussion

4.1 Effect measurement corrections on width to height ratio

The measured width and height of the trenches in sample (1) before and after the two methods of corrections discussed in section 3.2 are summarized in figure 4.1 . A transition from V-grooves to U-grooves takes place from an opening of around 650 nm in the SiO₂ mask. The maximum trench height is estimated by calculating the average height of the last 4 datapoints, which are (481 ± 2) nm, (482 ± 2) nm, before and after the correction respectively (note that both method I and method II correct the trench height in the same way). The width to height ratio of the trench is determined by performing a linear fit with the first six data points belonging to the V-groove region. The found values for these ratios are 1.55 ± 0.04 , 1.54 ± 0.09 , and 1.55 ± 0.04 for the uncorrected, method I, and method II data respectively.

The calculated correcting angles from method I are displayed in section 4.1. It appears that the uncertainty in these angles from this method are high, although it is significantly lower for larger trenches. From analyzing equations (C.6) and (C.7) in appendix C, it appears that the uncertainty in the measured trench width from both sideview and topview have a big contribution to the uncertainty in the correcting angles. In order to reduce this, the relative uncertainty of the trench width needs to be lower, either by using more accurate methods to measure with or by using larger trenches.

Comparing the raw data and two correction methods, the width to height ratio are also close to each other, which may mean that angle correction can be neglected in this case. The (mostly) low difference between the measured trench width from side and top view given in section 4.1 already suggests that corrections will end up small. Moreover, the correcting angles are most of the time smaller than their uncertainties. Therefore, it is not very useful to apply angle correction if the correcting angles are expected to be small with respect to their uncertainties, which would be the case in this experiment. The sample was tilted at only $\theta = (3 \pm 1)^\circ$ and placed as straight as possible so that $\phi \approx 0$. Furthermore, as explained in section 3.2, ψ is expected to be small with respect to the other angles.

However, all the results for the width to height ratio are higher than the expected value of $\sqrt{2} \approx 1.41$. Only looking at the value of the ratio for method I may imply that taking ψ into account may improve the final result, but this statement should be handled with caution because the uncertainty is too high. A more likely reason why the width to height ratio is too high, is the way how the SEM creates images. The problem is that the SiO₂ mask is a poor conductor and might build up charge when exposed to the electron beam. The charged SiO₂ can deflect the electrons from the beam and this would cause contraction along the height of the image (figure 4.2). This problem may be resolved by either using a coating that conducts the electricity better, or by using a doped InP substrate, which conducts electricity better and may help to discharge the mask. Drawback of the latter, however, is that etching of smooth {111}B facets will be more difficult.

Table 4.1: Overview of the method I calculated angles ϕ and ψ and their uncertainties s_ϕ and s_ψ , given the measured SiO₂ opening from topview w and its uncertainty s_w , the measured SiO₂ opening width w' from sideview and its uncertainty $s_{w'}$, and the measured angle α of the trench with respect to the normal of the cleaved surface and its uncertainty s_α .

$w \pm s_w$ (nm)	$w' \pm s_{w'}$ (nm)	$\alpha \pm s_\alpha$ (degrees)	$\phi \pm s_\phi$ (degrees)	$\psi \pm s_\psi$ (degrees)
402 ± 5	401 ± 5	58.0 ± 0.2	5 ± 12	0 ± 12
456 ± 5	461 ± 5	58.5 ± 0.2	-6 ± 11	11 ± 10
509 ± 5	508 ± 5	58.3 ± 0.2	3 ± 9	2 ± 9
563 ± 5	558 ± 5	57.5 ± 0.2	8 ± 9	-4 ± 9
612 ± 5	607 ± 5	57.1 ± 0.2	8 ± 8	-3 ± 8
660 ± 5	663 ± 5	58.3 ± 0.2	-1 ± 7	6 ± 7
713 ± 5	718 ± 5	57.5 ± 0.2	-2 ± 7	7 ± 7
761 ± 5	763 ± 5	57.3 ± 0.2	1 ± 7	4 ± 7
805 ± 5	804 ± 5	58.5 ± 0.2	3 ± 6	1 ± 6

4.2 MOVPE etching at center and edge of turning table

The average and SE of the width, height and width to height ratio of the trenches for both edge and center and for both 180 nm and 200 nm model openings are given in table 4.2. Some SEM images of these trenches are shown in figure 4.3. For the center sample, the width to height ratio appears to be in agreement with the expected value for both 180 nm and 200 nm model openings. For the edge sample, however, the width to height ratio appears to be higher than the expected value. The samples of edge and center were located at a different stub during SEMming, which may result in different conductivity and therefore a different charging deformation effect described in section 4.1. However, not the height, but the measured width of the edge samples is larger than those of the center samples. Because of this, it can be excluded that this is caused by contraction of the height due to charging as explained. On the other hand, this does not exclude the fact that the image may be deformed by expansion along the width, which will cause a higher width to height ratio as well. Angle correction along the width is not the most plausible solution. The reason is that this would mean that the width should be corrected by means of a high ψ , which is unlikely.

Another possible cause for this discrepancy could be that the V-groove may have a small {001} facet at the bottom of the trench. Wang et al. found these for V-grooves when photoresist masks were used and had a width of 20 nm to 40 nm [37]. It may be possible that the trenches in this experiment have such {001} facets as well. If they have about the same size as the ones reported by Wang et al., then it is expected that the trench should have been 14 nm to 28 nm higher if they would not be present. The width to height ratio for edge sample would be then 1.383-1.421 for 180 nm model openings and 1.389-1.428 for 200 nm model openings. Considering such a {001} facet does significantly affect the width to height ratio and for samples located at the edge, this would lead to the expected value. However, samples located at the center will probably have such a flat as well and correction will then lead to a width to height ratio that is too low.

Another possible explanation for this difference could be that the rotation flow of the sample at the edge of the disk is significantly higher, which increases the local airflow on this sample compared to the center one. The increased airflow could lead to a faster cleaning out of the InCl which might slightly change the etching rate of the side facets compared to the {001} facet.

4.3 Mapping in the AutoCAD model

A quick example of an AutoCAD mapping with topview images of sample (4) is shown in figure 4.4. The figure shows that the trenches are slightly overetched. The droplets seems to be placed properly

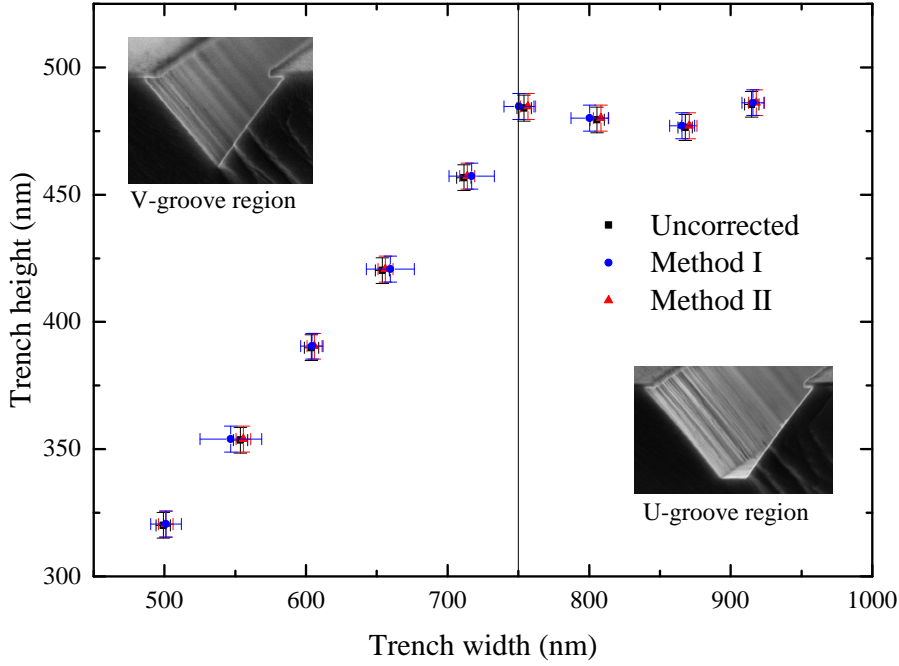


Figure 4.1: Plots of the trench width versus the trench height, uncorrected (black squares), corrected according to method I (blue circles), and corrected according to method II (red triangles). The figure shows a transition from V-grooves to U-grooves around 750 nm. Linear fit of the first 6 data points show that the width height ratio is 1.55 ± 0.04 , 1.55 ± 0.04 and 1.54 ± 0.09 for the uncorrected, method I, and method II data respectively. The data shows that correction does not lead to significant differences in the data

Table 4.2: average and SE of the width ($w \pm s_w$), height ($h \pm s_h$) and width to height ratio of the trenches for both edge and center and for both 180 nm and 200 nm model openings.

	$w \pm s_w$	$h \pm s_h$	width/height ratio
180 nm, center	694 ± 2	491 ± 1	1.414 ± 0.005
180 nm, edge	723 ± 3	492 ± 1	1.469 ± 0.006
200 nm, center	715 ± 3	506 ± 2	1.413 ± 0.009
200 nm, edge	739 ± 4	506 ± 1	1.460 ± 0.009

for these trenches, but because the trenches need to be smaller, it is better to place the outer droplets slightly closer to the opening. This is in particular the case for droplets on the left of the rightmost trench, because they are almost exactly in the middle between two trenches.

4.4 New kit issue of the MOVPE reactor

More results for the MOVPE reactor cannot be shown unfortunately. Since a new clean kit in the MOVPE reactor has been placed, the trenches coming from the reactor ended up asymmetric, irregular and with poor morphology (see figures 4.5a and 4.5b). The probable reason for this has been found when a wafer was put in the reactor without the addition of any HCl gas. After running the etching recipe without adding any HCl, the trenches were still partially etched, indicating that there is still some HCl gas in the chamber (see figure 4.5c). The cause of this may be the porous and uncoated graphite susceptor of the new clean kit. After etching with HCl gas, the graphite susceptor will absorb some leftover HCl gas. When a new sample will be loaded and the pressure in the chamber is reduced, HCl gas may diffuse out of the graphite susceptor and partially etch the new sample. A possible solution is to use a susceptor that is coated with SiC.

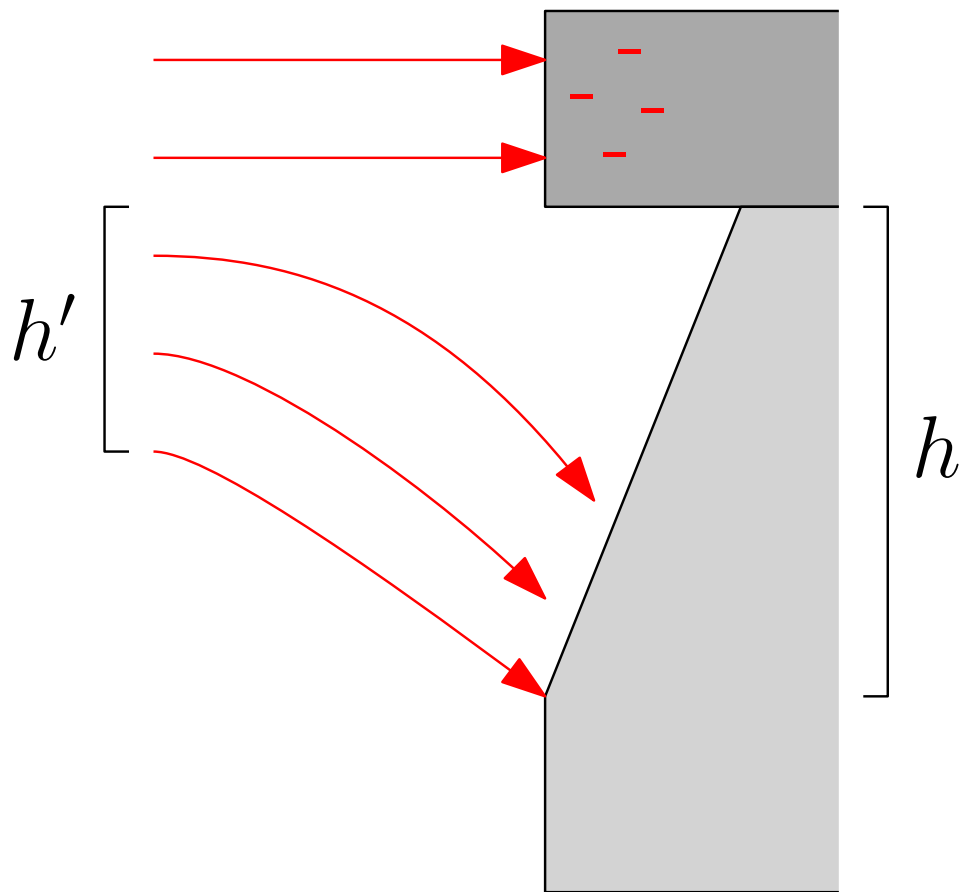
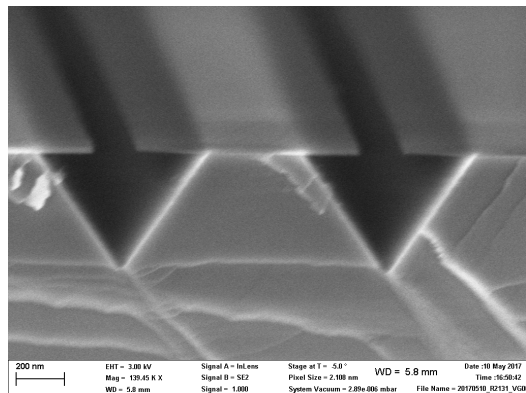
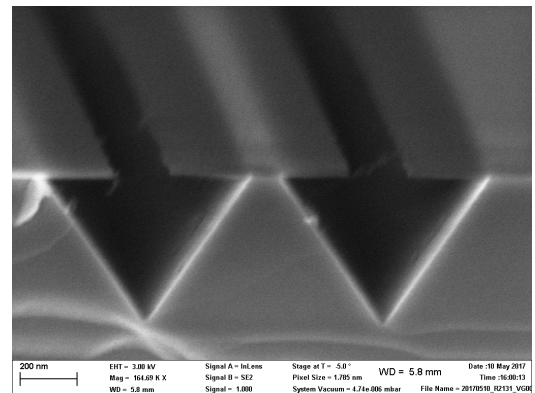


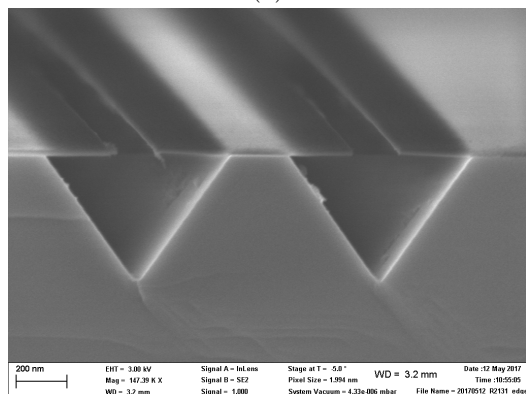
Figure 4.2: Visualization of height contraction of SEM images from h to h' .



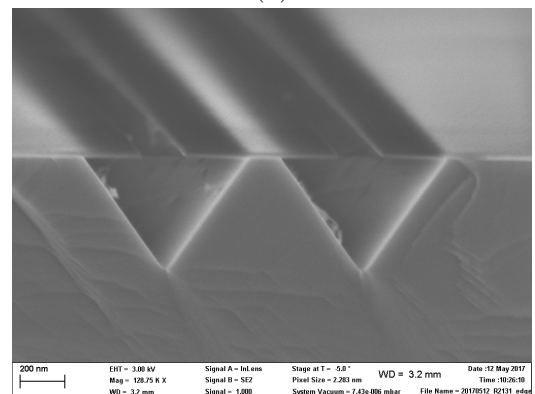
(a)



(b)



(c)



(d)

Figure 4.3: SEM images of trenches from (a) center, 180 nm; (b) center, 200 nm; (c) edge, 180 nm; and edge, 200 nm.

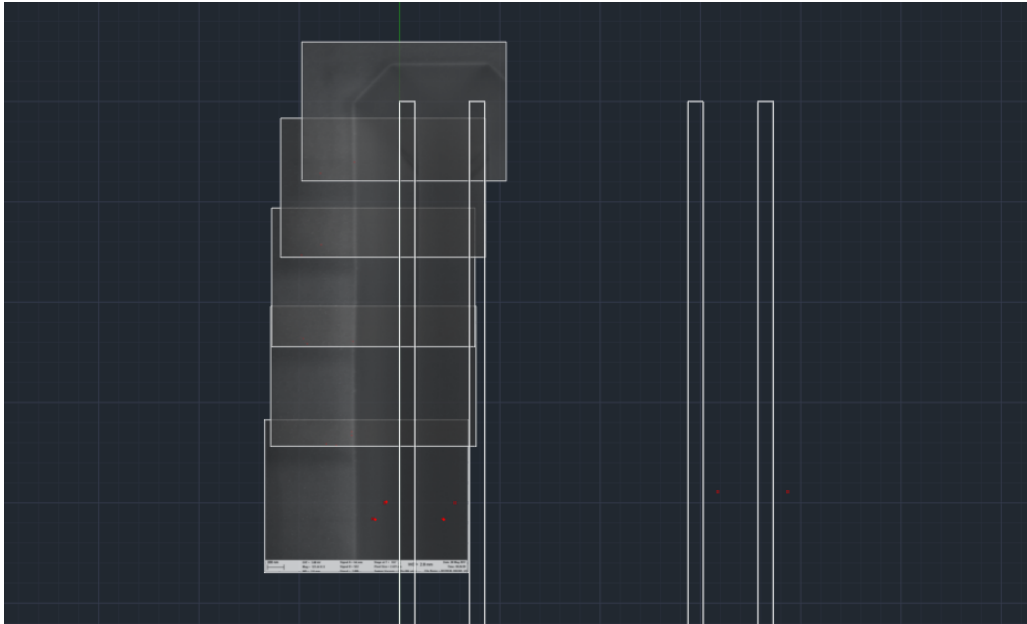
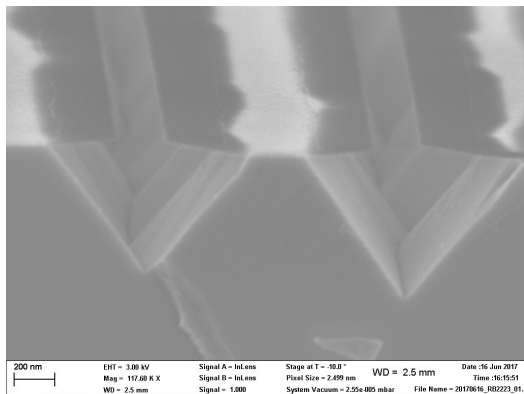
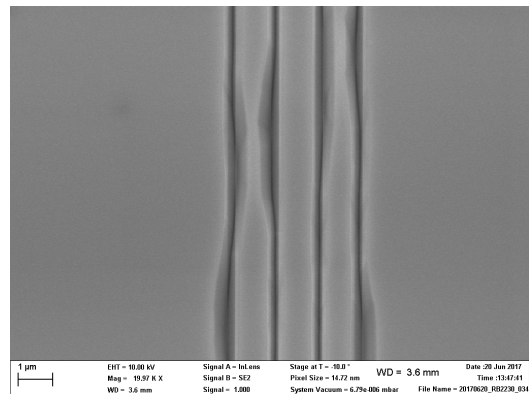


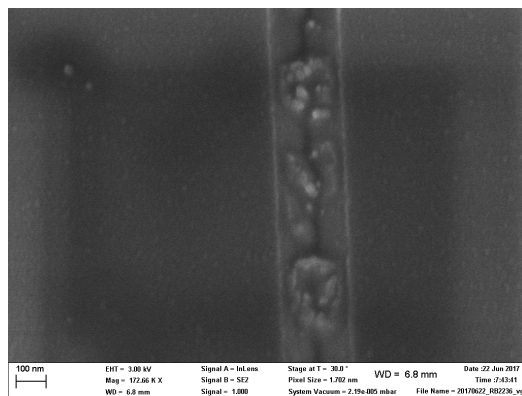
Figure 4.4: Mapping of SEM images on the AutoCAD model. The white lines indicate the trench opening and the red dots indicate the position of the gold droplets.



(a)



(b)



(c)

Figure 4.5: SEM figures of MOVPE etched trenches after the placement of a new clean kit. (a) Sideview for 5 cc HCl and 20 cc PH₃. (b) Topview for 2 cc HCl and 60 cc PH₃. (c) Topview for no HCl and 306 cc PH₃.

Chapter 5

Conclusion

Research on wet chemical etching and in-situ MOVPE etching have been reported. The purpose of this research is to optimize the etching process of trench etching. For wet chemical etching, the found width to height ratio is higher than the expected value. This is probably due to measurement errors and not because there is something wrong with the trenches themselves. The most likely reason is that the SEM images of the trenches are contracted in the height due to charging effects. The suggested solution is to use a conductive coating to reduce these effects. It may also help to use a doped InP substrate, which would conduct electricity better, but this may affect the surface morphology.

Two methods to correct width and height of the trenches have been proposed. It has been found that this method did not significantly affect the width to height ratio. It can be therefore concluded that, given the measurement uncertainties, the errors caused by these angles are negligibly small. Moreover, the first method (method I) shows high uncertainties in the correcting angles. The uncertainty in the trench width for both sideview and topview appear to be the main cause. Therefore, this method requires more accurate measurements in order to be reliable. Because it is the relative uncertainty in the width that causes this problem, wider trenches can resolve this as well, but this is for practical reasons not desired.

For MOVPE etching, it has been found that the sample positioned at the center of the rotation disk have the expected width to height ratio. For samples positioned at the edge, however, the width to height ratio is higher than expected. From the data, it is not likely that contraction of the height is the cause of this result, because the height for both edge and center appears to be the same. This suggested that the SEM images are expanded in the width instead of contracted in the height, but the exact cause cannot be determined with certainty. Method I could be used to correct the width to height ratio, but this would imply that the angle of the cleaved surface is high, which is not likely. Another cause of a high width to height ratio may be the presence of a small $\{001\}$ facet at the bottom of the 'V-groove', as reported by Wang et al. [37] If these facets were absent, then the samples at the edge may have the expected value of the width to height ratio, but samples at the center will have smaller width to height ratio if they have such facets as well. It is a good idea to zoom into the bottom of V-grooves to check for $\{001\}$ facets and to measure the width of them.

When the MOVPE reactor was producing undesired results after replacement of the kit, it took some time to find the possible cause. It was initially thought that mask misalignment along the $[110]$ direction was the cause. For such wet etched trenches, $\{1\bar{1}0\}$ facets become more visible when angle of misalignment along the $[110]$ direction becomes larger [20, 37]. Trenches will eventually have a rectangular etching profile if the angle becomes too large [37]. However, this effect was not visible after replacement of the kit. On the other hand, it is not explicitly found that mask misalignment will have the same effect for MOVPE etching and it is therefore worth checking it.

More experiments need to be done in order to get a better understanding of the trench etching process, although the timespan to perform this research was limited. Not only a different mask opening, but also a different temperatures and etching times should be tested for both etching methods. It is worth

investigating to check if the etch rates in all directions remain constant and if variations in temperature causes variations in the etch rate that are in agreement with Arrhenius equation (equation (2.2)). More import, it should also be found how good the surface morphologies are and how easy the results are to reproduce for different parameters. For wet etching, it is also worth to find out how H_3PO_4 content will affect the etching profile, which can neatly be displayed by using the model for anisotropic etching discussed in section 2.5. Also the usage of the SEM as measurement equipment requires attention, because it is not always clear why the width to height ratio differs from the expected value.

Bibliography

1. Lutchyn, R. M., Sau, J. D. & Sarma, S. D. Majorana Fermions and a Topological Phase Transition in Semiconductor-Superconductor Heterostructures. *Phys. Rev. Lett.* **105**, 077001 (2010).
2. Oreg, Y., Refael, G. & von Oppen, F. Helical Liquids and Majorana Bound States in Quantum Wires. *Phys. Rev. Lett.* **105**, 177002 (2010).
3. Mourik, V. *et al.* Signatures of Majorana Fermions in Hybrid Superconductor-Semiconductor Nanowire Devices. *Science* **336**, 1003–1007 (2012).
4. Zhang, H. *et al.* Ballistic Majorana nanowire devices. arXiv: 1603.04069 [cond-mat.mes-hall] (2016).
5. Deng, M. T. *et al.* Majorana bound state in a coupled quantum-dot hybrid-nanowire system. *Science* **354**, 1557–1562 (2016).
6. Albrecht, S. M. *et al.* Exponential protection of zero modes in Majorana islands. *Nature* **531**, 206–209 (2016).
7. Nilsson, H. A. *et al.* Giant, level-dependent g factors in InSb nanowire quantum dots. *Nano Lett.* **9**, 3151–3156 (2009).
8. Van Weperen, I. *et al.* Spin-orbit interaction in InSb nanowires. *Phys. Rev. B* **91**, 201413 (2015).
9. Kallaher, R. L., Heremans, J. J., Goel, N., Chung, S. J. & Santos, M. B. Spin-orbit interaction determined by antilocalization in an InSb quantum well. *Phys. Rev. B* **81**, 075303 (2010).
10. Alicea, J., Oreg, Y., Refael, G., von Oppen, F. & Fisher, M. P. A. Non-Abelian statistics and topological quantum information processing in 1D wire networks. *Nat. Phys.* **7**, 412–417 (2011).
11. Hyart, T. *et al.* Flux-controlled quantum computation with Majorana fermions. *Phys. Rev. B* **88**, 035121 (2013).
12. Aasen, D. *et al.* Milestones Toward Majorana-Based Quantum Computing. *Phys. Rev. X* **6**, 031016 (2016).
13. Plugge, S., Rasmussen, A., Egger, R. & Flensberg, K. Majorana box qubits. *New J. Phys.* **19**, 012001 (2017).
14. Vijay, S. & Fu, L. Teleportation-based quantum information processing with Majorana zero modes. *Phys. Rev. B* **94**, 235446 (2016).
15. Karzig, T. *et al.* Scalable Designs for Quasiparticle-Poisoning-Protected Topological Quantum Computation with Majorana Zero Modes. arXiv: 1610.05289 [cond-mat.mes-hall] (2016).
16. Plissard, S. R. *et al.* Formation and electronic properties of InSb nanocrosses. *Nat. Nanotechnol.* **8**, 859–864 (2013).
17. Car, D., Wang, J., Verheijen, M. A., Bakkers, E. P. A. M. & Plissard, S. R. Rationally Designed Single-Crystalline Nanowire Networks. *Adv. Mater.* **26**, 4875–4879 (2014).
18. Wang, J. *et al.* Reversible Switching of InP Nanowire Growth Direction by Catalyst Engineering. *Nano Lett.* **13**, 3802–3806 (2013).
19. Dalacu, D., Kam, A., Austing, D. G. & Poole, P. J. Droplet Dynamics in Controlled InAs Nanowire Interconnections. *Nano Lett.* **13**, 2676–2681 (2013).

20. Balk, S. C. *Fabrication methods for high yield Majorana braiding networks* Master (Delft University of Technology, 2016).
21. Car, D. *et al. Crossed InSb nanowire junctions for Majorana operations in Proceedings of the 28th International Conference on Indium Phosphide and Related Materials* (2016).
22. Gazibegovic, S. *et al. Epitaxy of Advanced Nanowire Quantum Devices*. arXiv: 1705.01480 [cond-mat.mes-hall] (2017).
23. Gatos, H. C. & Lavine, M. C. Characteristics of the {111} Surfaces of the III-V Intermetallic Compounds. *J. Chem. Phys.* **107**, 427–433 (1960).
24. Hiruma, K. *et al.* Growth and optical properties of nanometer-scale GaAs and InAs whiskers. *J. Appl. Phys.* **77**, 447–462 (1995).
25. Hatzakis, M. Electron Resists for Microcircuit and Mask Production. *J. Electrochem. Soc.* **116**, 1033–1037 (1969).
26. Nishida, T., Notomi, M., Iga, R. & Tamamura, T. Quantum Wire Fabrication by E-Beam Lithography Using High-Resolution and High-Sensitivity E-Beam Resist ZEP-520. *Jpn. J. Appl. Phys.* **31**, 4508–4514 (1992).
27. Raith GmbH. *EBPG5200* <https://www.raith.com/products/ebpg5200.html> (2017).
28. JEOL USA, Inc. *Electron Beam Lithography* <http://www.jeolusa.com/PRODUCTS/Photomask-Direct-Write-Lithography/Electron-Beam-Lithography> (2017).
29. Mapper Lithography B.V. *Introducing Mapper* <https://mapper.nl> (2017).
30. Lee, Y. H., Browning, R., Maluf, N., Owen, G. & Pease, R. F. W. Low voltage alternative for electron beam lithography. *J. Vac. Sci. Technol. B.* **10**, 3094–3098 (1992).
31. Yang, H. *et al. Low-energy Electron-beam Lithography of ZEP-520 Positive Resist in 1st IEEE International Conference on Nano/Micro Engineered and Molecular Systems* (2006), 391–394.
32. Kyser, D. F. & Viswanatham, N. Monte Carlo simulation of spatially distributed beams in electron-beam lithography. *J. Vac. Sci. Technol.* **12**, 1305–1308 (1975).
33. Kurogi, Y. Recent trends in dry etching. *Thin Solid Films* **92**, 33–40 (1982).
34. Klockenbrink, R., Peiner, E., Wehmann, H. H. & Schlachetzki, A. Wet Chemical Etching of Alignment V-Grooves in (100) InP through Titanium or In_{0.53}Ga_{0.47}As Masks. *J. Electrochem. Soc.* **141**, 1594–1599 (1994).
35. Kappelt, M. & Bimberg, D. Wet Chemical Etching of High Quality V-Grooves with {111}A Sidewalls on (001) InP. *J. Electrochem. Soc.* **143**, 3271–3273 (1996).
36. Adachi, S. & Kawaguchi, H. Chemical Etching Characteristics of (001)InP. *J. Electrochem. Soc.* **128**, 1342–1349 (1981).
37. Wang, J., Thompson, D. A. & Simmons, J. G. Wet Chemical Etching for V-grooves into InP Substrates. *J. Electrochem. Soc.* **145**, 2931–2937 (1998).
38. Huo, D. T. C., Wynn, J. D., Napholtz, S. G. & Wilt, D. P. Controlled Undercutting of V-Groove for InP by Photoresist Etch Mask. *J. Electrochem. Soc.* **135**, 1231–1234 (1988).
39. Studna, A. A. & Gualtieri, G. J. Optical properties and water absorption of anodically grown native oxides on InP. *Appl. Phys. Lett.* **39**, 965–966 (1981).
40. Wager, J. F. Composition and thermal stability of thin native oxides on InP. *J. Vac. Sci. Technol.* **19**, 513–518 (1981).
41. Dautremont-Smith, W. C. & Wilt, D. P. WO 86 /01367 (1986).
42. Turley, S. E. H. & Greene, P. D. LPE growth on structured {100} InP substrates and their fabrication by preferential etching. *J. Cryst. Growth* **58**, 409–416 (1982).
43. Phatak, S. B. & Kelner, G. Material-Selective Chemical Etching in the System InGaAsP / InP. *J. Electrochem. Soc.* **126**, 287–292 (1979).

44. Hjort, K. Sacrificial etching of III–V compounds for micromechanical devices. *J. Micromech. Microeng.* **6**, 370–375 (1996).
45. Seassal, C., Leclercq, J. L. & Viktorovitch, P. Fabrication of InP-based freestanding microstructures by selective surface micromachining. *J. Micromech. Microeng.* **6**, 261–265 (1996).
46. Notten, P. H. L. The Etching of InP in HCl Solutions: A Chemical Mechanism. *J. Electrochem. Soc.* **131**, 2641–2644 (1984).
47. Cuypers, D., Gendt, S. D., Arnauts, S., Paulussen, K. & van Dorp, D. H. Wet Chemical Etching of InP for Cleaning Applications: I. An Oxide Formation/Oxide Dissolution Model. *J. Solid State Sci. Technol.* **2**, 185–189 (2013).
48. Agnello, P. D. & Ghandhi, S. K. In-situ etching of InP by a low pressure transient HCL process. *J. Cryst. Growth* **73**, 453–459 (1985).
49. Gessner, R., Dobbins, A., Rieger, J. & Veuhoff, E. Fabrication of AlGaInAs and GaInAsP buried heterostructure lasers by in situ etching. *J. Cryst. Growth* **248**, 426–430 (2003).
50. Wolfram, P., Franke, D., Ebert, W. & Grote, N. MOVPE-based in-situ etching of InP epitaxial heterostructures in *Proceedings of the 14th International Conference on Indium Phosphide and Related Materials* (2002), 331–334.
51. Gessner, R. *et al.* In-situ etching of InP based BH laser structures in MOVPE in *Proceedings of the 13th International Conference on Indium Phosphide and Related Materials* (2001), 398–400.
52. Tsang, W. T., Kapre, R. & Jr., P. F. S. Reactive chemical beam etching of InP inside a chemical beam epitaxial growth chamber using phosphorus trichloride. *Appl. Phys. Lett.* **62**, 2084–2086 (1993).
53. Ougazzaden, A., Peticolas, L., Radar, M. & Chu, S. N. G. In-situ etching of InP and related P materials in MOVPE chamber using PCl₃ in *Proceedings of the 14th International Conference on Indium Phosphide and Related Materials* (2002), 327–330.
54. Clawson, A. R. In situ vapor-etch for InP MOVPE using ethylene dibromide. *J. Cryst. Growth* **69**, 346–356 (1984).
55. Caneau, C., Bhat, R., Koza, M., Hayes, J. R. & Esagui, R. Etching of InP by HCL in an OMVPE reactor. *J. Cryst. Growth* **107**, 203–208 (1991).
56. Sangster, R. C. *Compound Semiconductors, Vol. 1, Preparation of III-V Compounds* (Reinhold Publishing Corporation, Reinhold, NY, 1962).
57. Tsuchiya, T., Kitatani, T., Ouchi, K., Sato, H. & Aoki, M. In-situ etching of InP and InGaAlAs materials by using HCl gas in metalorganic vapor-phase epitaxy. *J. Cryst. Growth* **272**, 125–130 (2004).
58. Kitatani, T., Tsuchiya, T., Shinoda, K. & Aoki, M. In situ etching of InGaAsP/InP by using HCl in an MOVPE reactor. *J. Cryst. Growth* **274**, 372–378 (2005).
59. Shaw, D. W. Morphology analysis in localized crystal growth and dissolution. *J. Cryst. Growth* **47**, 509–517 (1979).

Appendix A

Width height ratio of V-grooves

ZB is based on cubic crystals and the corresponding $\{111\}$ B plane is visualized in figure 2.1. The sideview of a V-groove is given by the cross section of the $\{111\}$ B plane along the $\{110\}$ plane. The width height ratio of the V-groove is therefore the width height ratio of the $\{110\}$ plane inside the cube, which is $\sqrt{2}$. Usually, literature states that a $\{111\}$ B plane form an angle of 54.7° with respect to the $\{001\}$ plane, or that two opposing $\{111\}$ B planes form an angle of 70.5° . Trigonometry shows that

$$\arctan \sqrt{2} \approx 54.7^\circ, \quad (\text{A.1})$$

and

$$2 \arctan \frac{1}{\sqrt{2}} \approx 70.5^\circ. \quad (\text{A.2})$$

Thus, for perfect V-grooves, these two statements are equivalent to the statement that the width to height ratio is $\sqrt{2}$.

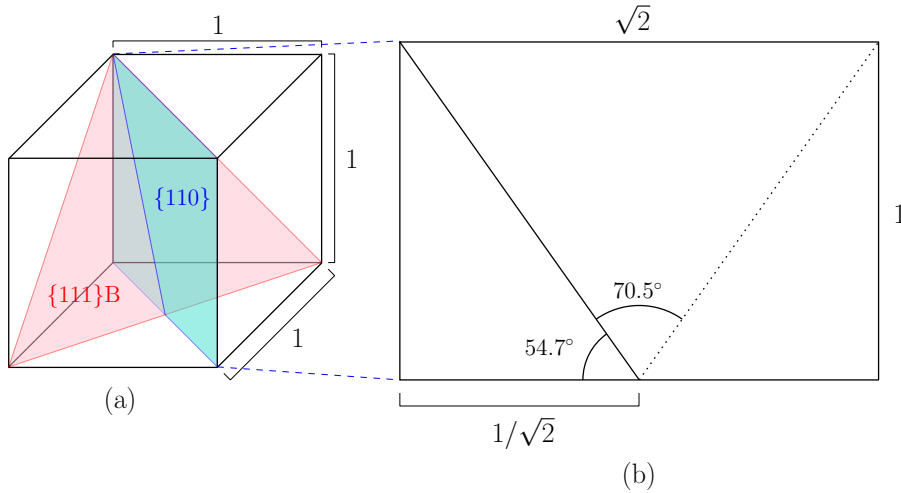


Figure A.1: Visualization of a $\{111\}$ B plane in ZB, with (a) the overall situation and (b) the cross section along the $\{110\}$ plane.

Appendix B

Derivation of Shaw's formula on etch rate

Given are the etch rates $r(\Theta_1)$ and $r(\Theta_2)$, where $\Theta_1 < \Theta_2$. An illustration of the problem is given in figure B.1. In the figure, note that $\angle OAI$ and $\angle OBI$ are right angles and are opposing angles in the quadrilateral $O A I B$. Therefore, $O A I B$ has to be a cyclic quadrilateral and its corresponding circumscribed circle with center C is drawn in the figure. Because $O I$ is the hypotenuse of the right triangle $O A I$, $O I$ has to be the diameter D of the circumscribed circle according to the converse of Thales's theorem. The same can be applied for triangle $O M I$ and this implies that the inscribed circle of $O M I$ is the same as that of $O A I$. As a result, M should lie on the circumscribed circle of the quadrilateral $O A I B$ because it is the same one as that of $O A I$.

The diameter of a circumscribed circle can also be calculated by using the law of sines. For the triangles $O A B$, $O A M$, and $O B M$ the formula is

$$D = \frac{AB}{\sin(\Theta_2 - \Theta_1)} = \frac{AM}{\sin(\Theta_i - \Theta_1)} = \frac{BM}{\sin(\Theta_2 - \Theta_i)}. \quad (\text{B.1})$$

AB , AM , and BM can be calculated by means of the law of cosines:

$$AB^2 = r(\Theta_2)^2 + r(\Theta_1)^2 - 2r(\Theta_1)r(\Theta_2)\cos(\Theta_2 - \Theta_1), \quad (\text{B.2})$$

$$AM^2 = r(\Theta_1)^2 + r(\Theta_i)^2 - 2r(\Theta_1)r(\Theta_i)\cos(\Theta_i - \Theta_1), \quad (\text{B.3})$$

$$BM^2 = r(\Theta_i)^2 + r(\Theta_2)^2 - 2r(\Theta_i)r(\Theta_2)\cos(\Theta_2 - \Theta_i). \quad (\text{B.4})$$

Plugging equations (B.2) to (B.4) into equation (B.1) and rearranging gives the following two equations:

$$\begin{aligned} r(\Theta_i)^2 - 2r(\Theta_1)\cos(\Theta_i - \Theta_1)r(\Theta_i) + r(\Theta_1)^2 = \\ \left(\frac{\sin(\Theta_i - \Theta_1)}{\sin(\Theta_2 - \Theta_1)}\right)^2 \left(r(\Theta_1)^2 + r(\Theta_2)^2 - 2r(\Theta_1)r(\Theta_2)\cos(\Theta_2 - \Theta_1)\right), \end{aligned} \quad (\text{B.5})$$

$$\begin{aligned} r(\Theta_i)^2 - 2r(\Theta_2)\cos(\Theta_2 - \Theta_i)r(\Theta_i) + r(\Theta_2)^2 = \\ \left(\frac{\sin(\Theta_2 - \Theta_i)}{\sin(\Theta_2 - \Theta_1)}\right)^2 \left(r(\Theta_1)^2 + r(\Theta_2)^2 - 2r(\Theta_1)r(\Theta_2)\cos(\Theta_2 - \Theta_1)\right), \end{aligned} \quad (\text{B.6})$$

which are both quadratic equations with respect to $r(\Theta_i)$. Only solutions that result from both equation (B.5) and equation (B.6) are valid and thus the only solution is given by

$$\boxed{r(\Theta_i) = \frac{r(\Theta_1)\sin(\Theta_2 - \Theta_i) + r(\Theta_2)\sin(\Theta_i - \Theta_1)}{\sin(\Theta_2 - \Theta_1)}}. \quad (\text{B.7})$$

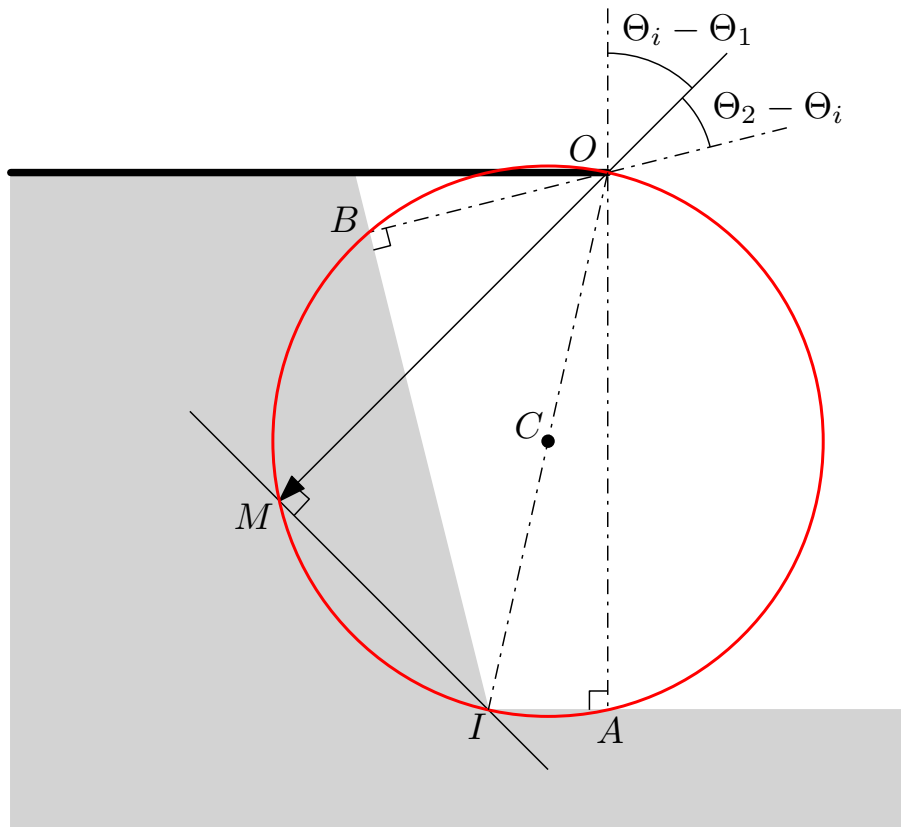


Figure B.1: Visualization of derivation of minimum etch rate formula of Shaw [59]. Note that $OA = r(\Theta_1)$, $OB = r(\Theta_2)$ and $OM = r(\Theta_i)$. A more detailed explanation can be found in the text.

Appendix C

The Newton-Raphson method

The Newton-Raphson method is a numeric method that is used to find a root of a function $f(x) = 0$. The method starts with an initial guess x_0 and calculates a better guess x_1 according to

$$x_1 = x_0 - \frac{f(x_0)}{f'(x_0)}, \quad (\text{C.1})$$

where f' indicates the derivative of a function. This process will be repeated until a sufficiently accurate value is found. The Newton-Raphson method can also be used to solve nonlinear systems of equations ($F^i(x^j) = 0$). In that case, equation (C.1) can be rewritten in tensor calculus notation as

$$J_j^i(x_{(n)}^j) (x_{(n+1)}^j - x_{(n)}^j) = -F^i(x_{(n)}^j), \quad (\text{C.2})$$

where $J_j^i = \partial F^i / \partial x^j$ is the Jacobian tensor, $x_{(n)}^j$ the values of the old guess, $x_{(n+1)}^j$ the values of the new guess. This method can be used to calculate the angles discussed in section 3.2. The Jacobian tensor in this problem is

$$J_j^i = \begin{pmatrix} \frac{1}{\cos^2(\phi+\psi)} & 0 & \frac{1}{\cos^2(\phi+\psi)} \\ \frac{1}{\cos^2(\phi)} & -\frac{\sin \theta}{\cos^2(\phi')} & 0 \\ w' \frac{\sin \phi \cos \psi}{\cos^2 \phi} & 0 & -w' \frac{\sin \psi}{\cos \phi} \end{pmatrix}. \quad (\text{C.3})$$

Note that if ϕ and ψ are both zero, the third row of the Jacobian tensor becomes zero and the tensor will become singular. A MATLAB script is written to calculate the correcting angles using the Newton-Raphson method and the code is given in section C.1. The method is also used in the `FindRoot` function of Wolfram-Mathematica 11.0 and it verifies the output given by the MATLAB script.

The (sampling) standard deviation s_ϕ and s_ψ in the calculated angles ϕ and ψ are related to the standard deviations in α , θ , w and w' (s_α , s_θ , s_w and $s_{w'}$ respectively) according to

$$s_\phi^2 = \left(\frac{\partial \phi}{\partial \alpha} s_\alpha \right)^2 + \left(\frac{\partial \phi}{\partial \theta} s_\theta \right)^2 + \left(\frac{\partial \phi}{\partial w} s_w \right)^2 + \left(\frac{\partial \phi}{\partial w'} s_{w'} \right)^2, \quad (\text{C.4})$$

$$s_\psi^2 = \left(\frac{\partial \psi}{\partial \alpha} s_\alpha \right)^2 + \left(\frac{\partial \psi}{\partial \theta} s_\theta \right)^2 + \left(\frac{\partial \psi}{\partial w} s_w \right)^2 + \left(\frac{\partial \psi}{\partial w'} s_{w'} \right)^2. \quad (\text{C.5})$$

Because the derivatives in the equations are constant for sufficiently small standard deviations, the computation can be simplified to

$$s_\phi^2 = [\phi(\alpha, \theta, w, w') - \phi(\alpha + s_\alpha, \theta, w, w')]^2 + [\phi(\alpha, \theta, w, w') - \phi(\alpha, \theta + s_\theta, w, w')]^2 \\ + [\phi(\alpha, \theta, w, w') - \phi(\alpha, \theta, w + s_w, w')]^2 + [\phi(\alpha, \theta, w, w') - \phi(\alpha, \theta, w, w' + s_{w'})]^2, \quad (\text{C.6})$$

$$s_\psi^2 = [\psi(\alpha, \theta, w, w') - \psi(\alpha + s_\alpha, \theta, w, w')]^2 + [\psi(\alpha, \theta, w, w') - \psi(\alpha, \theta + s_\theta, w, w')]^2 \\ + [\psi(\alpha, \theta, w, w') - \psi(\alpha, \theta, w + s_w, w')]^2 + [\psi(\alpha, \theta, w, w') - \psi(\alpha, \theta, w, w' + s_{w'})]^2, \quad (\text{C.7})$$

where $\phi(\alpha, \theta, w, w')$ and $\psi(\alpha, \theta, w, w')$ indicate the solution of the system for the given α , θ , w , and w' .

C.1 MATLAB scripts

Find root function

This script describes a MATLAB functions that finds the root of the equations for the correcting angles shown in section 3.2.

```
1 function [phi,psi] = findroot(alpha,w,wpr,theta)
2     phi = 0; % Initial guess phi
3     psi = 0.2; % Initial guess psi
4     phipr = 0; % Initial guess phi'
5     delta = [999999999; 999999999; 999999999];
6     % Difference with respect to initial guess, initally set high
7     % because
8     % there was no guess before.
9
10    iterations = 0; % Count number of iterations.
11    % Iterate until difference between old and new guess are small.
12    while abs(delta(1)) > 1e-6 || abs(delta(2)) > 1e-6 || abs(delta(3)
13        ) > 1e-6
14        % Calculate jacobian
15        J = [1/cos(phi+psi)^2 0 1/cos(phi+psi)^2;
16            1/cos(phi)^2 -sin(theta)/cos(phipr)^2 0;
17            -wpr*sin(phi)*cos(psi)/cos(phi)^2 0 wpr*sin(psi)/cos(phi)
18            ];
19
20        % Calculate functions where you want to find a root.
21        F = -[tan(phi+psi)-tan(alpha)*sin(theta);
22            tan(phi)-tan(phipr)*sin(theta);
23            w-wpr*cos(psi)/cos(phi)];
24
25        % Calculate new differences.
26        delta = J\F;
27
28        % update new guesses.
29        phi = phi + delta(1); phipr = phipr + delta(2); psi = psi +
30            delta(3);
31
32        iterations = iterations + 1; % increase iteration counter.
33        % In case it get stuck in infinite iterations due to, e.g.,
34        % almost-singularity.
35        if iterations >= 10000
36            break
37        end
38    end
39 end
```

Calculate corrections script

This script corrects the given measured trench width and height and outputs the corrected dimensions using equation (3.5) and equation (3.2) for width and height respectively.

```
1 % Input CSV file:
```

```

2 % Trench width model, measured width SiO opening, measured trench
   width,
3 % measured trench height, uncertainty SEM measurement, theta, s_theta,
4 % alpha, s_alpha.
5 %
6 % Angles in the input file should be given in degrees.
7 %
8 % Output CSV file:s
9 % Trench width model, measured width SiO opening, measured trench
   width,
10 % measured trench height, uncertainty SEM measurement, theta, s_theta,
11 % alpha, s_alpha, phi, s_phi, psi, s_psi, w_corr, s_w_corr, h_corr,
12 % s_h_corr.
13
14 inputfilename = input('Enter inputfilename: ');
15 outputfilename = input('Enter outputfilename: ');
16
17 % Put CSV file into matrix.
18 M = csvread(inputfilename);
19
20 % Create vector for the new columns.
21 phicol = zeros(numel(M)/9,1);
22 s_phicol = zeros(numel(M)/9,1);
23 psicol = zeros(numel(M)/9,1);
24 s_psicol = zeros(numel(M)/9,1);
25 w_corrcol = zeros(numel(M)/9,1);
26 s_w_corrcol = zeros(numel(M)/9,1);
27 h_corrcol = zeros(numel(M)/9,1);
28 s_h_corrcol = zeros(numel(M)/9,1);
29
30 for i=1:numel(M)/9
31     % Give columns sensible variable names.
32     w = M(i,1); open = M(i,2); wpr = M(i,3); h = M(i,4); ds = M(i,5);
33     theta = M(i,6)*pi/180; s_theta = M(i,7)*pi/180; alpha = M(i,8)*pi
        /180;
34     s_alpha = M(i,9)*pi/180;
35
36     % Calculate solution of problem, including uncertainties.
37     [phi,psi] = findroot(alpha, w, open, theta);
38     [sphi1,spsi1] = findroot(alpha+s_alpha, w, open, theta);
39     [sphi2,spsi2] = findroot(alpha, w, open+ds, theta);
40     [sphi3,spsi3] = findroot(alpha, w, open, theta+s_theta);
41     [sphi4,spsi4] = findroot(alpha, w+ds, open, theta);
42
43     % Calculate phi and psi, needed to calculate trench width.
44     phicol(i) = phi; psicol(i) = psi;
45     s_phicol(i) = sqrt((phi-sphi1)^2+(phi-sphi2)^2+(phi-sphi3)^2+(phi-
        sphi4)^2);
46     s_psicol(i) = sqrt((psi-spsi1)^2+(psi-spsi2)^2+(psi-spsi3)^2+(psi-
        spsi4)^2);
47
48     % Calculate trench height and uncertainty.
49     h_corrcol(i) = h/cos(theta);

```

```

50     s_h_corrcol(i) = sqrt( ds^2/cos(theta)^2 + (sin(theta)*h*s_theta)
      ^2/cos(theta)^4);
51
52     % Calculate trench width and uncertainty.
53     w_corrcol(i) = wpr*cos(psi)/cos(phi);
54     coef1 = cos(psi)/cos(phi)*ds;
55     coef2 = sin(psi)/cos(phi)*s_psicol(i)*wpr;
56     coef3 = sin(phi)*cos(psi)/cos(phi)^2*s_phicol(i)*wpr;
57     s_w_corrcol(i) = sqrt(coef1^2+coef2^2+coef3^2);
58 end
59
60 % Convert angles of phi and psi into degrees.
61 phicol = phicol.*180./pi; s_phicol = s_phicol.*180./pi;
62 psicol = psicol.*180./pi; s_psicol = s_psicol.*180./pi;
63
64 % Create output matrix from columns and write it to csv file.
65 Mout = [M phicol s_phicol psicol s_psicol w_corrcol s_w_corrcol
      h_corrcol s_h_corrcol];
66 csvwrite(outputfilename,Mout);

```